Water Resources Research

RESEARCH ARTICLE
10.1029/2023WR036031

Exploring the Influence of Morphologic Heterogeneity and Discharge on Transient Storage in Stream Systems: 1. Insights From the Field

Ian Gambill[1], **Anna Marshall**[2,3], **David A. Benson**[1], **Sawyer McFadden**[1], **Alexis Navarre-Sitchler**[1], **Ellen Wohl**[2], **and Kamini Singha**[1]

[1]Hydrologic Science and Engineering Program, Geology and Geological Engineering Department, Colorado School of Mines, Golden, CO, USA, [2]Department of Geosciences, Colorado State University, Fort Collins, CO, USA, [3]Department of Geography & Sustainability, University of Tennessee, Knoxville, TN, USA

Key Points:

- Logjams drive surface transient storage through backwater pools that increase with discharge, which in turn drive subsurface exchange
- Intermittent secondary channels increase additional opportunities for surface and subsurface transient storage
- Increasing discharge affects transient storage, decreasing retention in surface water and causing non-linear subsurface retention

Supporting Information:

Supporting Information may be found in the online version of this article.

Correspondence to:

I. Gambill,
ian.gambill@gmail.com

Citation:

Gambill, I., Marshall, A., Benson, D. A., McFadden, S., Navarre-Sitchler, A., Wohl, E., & Singha, K. (2025). Exploring the influence of morphologic heterogeneity and discharge on transient storage in stream systems: 1. Insights from the field. *Water Resources Research*, *61*, e2023WR036031. https://doi.org/10.1029/2023WR036031

Received 7 AUG 2023
Accepted 27 DEC 2024

Author Contributions:

Conceptualization: Ellen Wohl, Kamini Singha
Data curation: Ian Gambill
Formal analysis: Ian Gambill, David A. Benson, Kamini Singha
Funding acquisition: Alexis Navarre-Sitchler, Ellen Wohl, Kamini Singha
Investigation: Ian Gambill, Anna Marshall, Sawyer McFadden, Ellen Wohl, Kamini Singha
Methodology: Ian Gambill, David A. Benson, Ellen Wohl, Kamini Singha
Project administration: Kamini Singha

Abstract

Here, we explore how differences in morphologic heterogeneity due to logjams and secondary channels drive transient storage across discharge in two stream reaches within the Front Range of Colorado, USA. During three tracer tests conducted from baseflow to near-peak snowmelt, we collected instream fluid conductivity measurements and conducted electrical resistivity surveys to characterize tracer movement in the surface and subsurface of the stream system. The reach with two logjams and an intermittent secondary channel exhibited greater heterogeneity in surface transient storage, driving heterogeneity in hyporheic exchange flows, compared to the reach with a single logjam and a perennial secondary channel. As discharge increased, (a) backwater pools created by logjams increased in size in both systems, (b) channel complexity increased as logjams forced flow into secondary channels, and (c) subsurface flowpath distribution increased. Various transient storage indices provide some insight on solute retention but compressing data from this system into simple values was unintuitive given the noise in breakthrough-curve tails and secondary peaks in concentration. While subsurface exchange increases with discharge in both reaches, retention may not. Flushing of subsurface tracers is highest at medium discharge as interpreted from the electrical resistivity inversions in both reaches, perhaps because of a tradeoff between the increasing extent of subsurface flowpaths with discharge and larger pressure gradients for driving flow. This work is one of the first to explore controls on exchange and retention in stream systems with multiple logjams and evolving channel planform using geophysical data to constrain the subsurface movement of solutes.

Plain Language Summary

Transient storage refers to the short-term retention of water and dissolved substances within a stream system. It keeps rivers and streams healthy by regulating temperature, oxygen, and nutrients. Logjams make transient storage complex by driving water into the subsurface, changing how streams are connected to the floodplain, and generating surface storage through backwater pools. Many studies of such storage to date have focused on single logjams or laboratory experiments. Here, we use innovative hydrologic tools to study the effect of logjams on transient storage in a complex environment with two logjams and multiple channels, where one secondary channel was dry in the early season and flowing at later times. We find more surface transient storage and subsurface exchange at higher streamflow as logjams create more or larger backwater pools, complex channels, and flowpaths, allowing for greater interactions between the stream and the subsurface. In this work, we address a gap in research by providing insight on how logjams and inconsistent flow in a secondary stream channel control solute transport in a complex stream.

1. Introduction

The exchange of water in rivers between (a) stream channels, (b) low-velocity zones (e.g., surface-water dead zones, backwater pools, and eddies), and (c) streambed sediments are jointly referred to as transient storage (Mason et al., 2012). The processes involved in transient storage refer to exchanges over short timescales (i.e., minutes to weeks; Magliozzi et al., 2018). Transient storage can generally be classified as surface transient storage—where water flows in low-velocity zones within the stream channel—or subsurface transient storage—where surface water flows into the porous subsurface alluvium and eventually returns to the stream. Hyporheic exchange flow (HEF) refers to the movement of water and dissolved substances between surface water and groundwater in the hyporheic zone, the transitional area between the river water and shallow groundwater (Ward et al., 2010a). Both surface and subsurface transient storage play a crucial role in maintaining the health of rivers and streams by

Resources: Ellen Wohl, Kamini Singha
Supervision: Kamini Singha
Validation: Alexis Navarre-Sitchler, Kamini Singha
Visualization: Ian Gambill
Writing – original draft: Ian Gambill
Writing – review & editing: Ian Gambill, Anna Marshall, David A. Benson, Sawyer McFadden, Alexis Navarre-Sitchler, Ellen Wohl, Kamini Singha

regulating water temperature (Sawyer & Cardenas, 2012), oxygen levels (Kaufman et al., 2017), and the availability of nutrients and other dissolved substances (Marzadri et al., 2016; Tonina & Buffington, 2009). Subsurface transient storage also helps to filter or transform pollutants and other contaminants (Fischer et al., 2005; Hoagland et al., 2020). The magnitude and extent of transient storage is driven by potential- and kinetic-energy gradients (Magliozzi et al., 2018), which are controlled by geologic heterogeneity (Gooseff et al., 2007; Salehin et al., 2004), changes in discharge (Tonina & Buffington, 2011), turbulence (Grant et al., 2018), channel morphology (Livers & Wohl, 2016), bed topography (Marzadri et al., 2014), and obstructions like large wood (defined as woody material >10 cm in diameter and 1 m in length) or logjams within the stream (Ader et al., 2021; Buffington & Tonina, 2009; Sawyer et al., 2011; Wohl, 2017).

Individual pieces of large wood and logjams (defined as a collection of ≥3 large wood pieces) play a critical role in surface and subsurface transient storage and overall stream function. In reaches with channel-spanning logjams, low-velocity backwaters can form upstream of the obstruction (e.g., Beckman & Wohl, 2014; Gippel, 1995; Wohl et al., 2022), leading to heightened water surface elevation that generates increased pressure and consequent hyporheic downwelling in the bed upstream of the jam and return flow in the scour pool downstream of the jam (Livers & Wohl, 2016; Tonina & Buffington, 2011; Wohl et al., 2022). Large wood can also redirect flow towards the channel bed, which creates scour pools that allow for larger residual pool volume (e.g., Mao et al., 2008) and flow heterogeneity between multiple logs (Shalko et al., 2024; Zhang et al., 2020). Logjams also promote channel complexity through the formation of multi-channel planform (the divergence of a stream into multiple channels and subsequent reconvergence into a single channel downstream), enhanced overbank flow and channel-floodplain connectivity, and channel migration (Livers & Wohl, 2016; Magliozzi et al., 2018; Wohl et al., 2022). Historically, large wood has been removed from streams for navigation, transportation of timber, and flood control, thereby compromising channel complexity and associated surface and subsurface storage (Sawyer et al., 2011; Wohl, 2005, 2006, 2014).

Researchers use several methods to quantify transient storage in stream systems, including instream solute breakthrough curves (BTCs) from tracer tests. The temporal analysis of BTCs can help differentiate dominant transport processes in streams (Gonzalez-Pinzon et al., 2013; Gupta & Cvetkovic, 2000; Ward et al., 2013; Wlostowski et al., 2017). For surface transient storage, methods like signal deconvolution have been used (e.g., Cirpka et al., 2007; Gooseff et al., 2011). Meanwhile, electrical resistivity (ER) imaging with tracer injection has provided detailed, multi-dimensional, spatial data (e.g., Ward et al., 2010a, 2010b) and for estimating the size and timescales of hyporheic exchange in the subsurface (Singley et al., 2022).

Although past studies have examined the effect of logjams on transient storage, they have mostly focused on artificial or relatively simple natural structures. Work by Doughty et al. (2020) was one of the first to use combined tracer injection and electrical resistivity (ER) imaging to observe HEF around a natural channel-spanning logjam. Their work demonstrated that (a) HEF was higher in a reach with a channel-spanning logjam than in a reach without, (b) logjams increased solute retention, and (c) higher discharge rates amplified the magnitude and extent of HEF (Doughty et al., 2020). Similarly, Sawyer et al. (2011) investigated the effect of a single, channel-spanning log on HEF using flume experiments and numerical modeling and found that HEF rates were highest near the log and decreased exponentially with distance upstream and downstream.

Because most studies focus on simple systems, it is poorly understood whether multiple logjams (here, meaning multiple independent agglomerations of wood (jams) along a stream) generate an additive or reduced effect on transient storage and HEF, especially in field settings. It is possible that logjams may synergistically increase HEF by maintaining relatively higher water elevations across multiple channels than streams with simpler morphology, which could create stronger pressure gradients for HEF. In areas where multiple channels split surface flow around logjams, overtopping of water across the logjams may be less prevalent, allowing logjams to enhance the percent of discharge that is driven into the subsurface. Increased logjam-distribution density, defined as the number of logjams per channel length, may create conditions that enhance hydraulic roughness and overbank flow (Wohl & Scamardo, 2021). Despite significant progress in characterizing morphologic controls on solute transport, there are few studies that examine the influence of multiple logjams on HEF in natural stream systems, especially with the added complication of stream intermittency.

Given the challenges of teasing apart complex systems, especially subsurface controls, we rely on a multi-part approach that uses field, flume, and numerical modeling methods to examine surface and subsurface interactions, as suggested by Krause et al. (2022). Here, we explore the field component, noting that the work presented here is part of a larger effort, with prior studies examining different aspects of the problem in field and flume settings, such as to role of channel slope (Ader et al., 2021), channel planform (Wilhelmsen et al., 2021), logjam porosity and density (Marshall et al., 2023), and discharge (Doughty et al., 2020) on hyporheic exchange. Wilhelmsen et al. (2021) found that jams increased connectivity between the stream and shallow groundwater based on flume experiments and numerical modeling, extending flowpath lengths within the hyporheic zone, especially where multiple jams were present, and increased the amount of time water spends in the hyporheic zone as it flows downstream with respect to the time required for chemical transformations. In Marshall et al. (2023), we explored how logjam distribution density, logjam permeability, and discharge influence transient storage in a flume. These results showed that stream segments with multiple, successive logjams increased the extent of the hyporheic zone relative to stream segments with fewer logjams, thereby increasing HEF. Additionally, those findings showed that higher discharge or decreased permeability of the logjams generated more HEF.

To build on this previous work, here we investigate how morphologic heterogeneity in the form of multiple logjams and intermittent secondary channels influence transient storage. We collect data on surface and subsurface transient storage at different stream discharges in two reaches of Little Beaver Creek, in northern Colorado, USA, the same site that Doughty et al. (2020) studied. We hypothesize that (a) the reach with two logjams and an intermittent secondary channel would exhibit greater variability in advective pathways and surface and subsurface retention compared to the reach with a single logjam and a perennial secondary channel and (b) transient storage in both the surface and subsurface will decrease with increasing discharge in both reaches. To test our hypotheses, we conducted saline tracer tests to measure solute transport via instream electrical conductivity (EC) and bulk electrical resistivity (ER, for imaging subsurface movement of the tracer) at three discharges ranging from baseflow to near-peak snowmelt. Results from this study are bolstered by a companion paper, Zhang et al. (n.d.), that describes HydroGeoSphere models that seek to further explain these field data and extend our understanding of this system beyond the limited measurements that can be made in the field. By characterizing transient storage in multi-channel reaches with logjams and secondary channels, this study fills a critical gap in exploring how logjams and stream intermittency impact HEF in a natural, complex system, and our ability to quantify them.

2. Methods

2.1. Little Beaver Creek, Colorado, USA

We performed our experiments in Little Beaver Creek, a third-order tributary of the South Fork Cache la Poudre River in northern Colorado, USA (Figure 1). Little Beaver Creek is a sand-to cobble-bedded stream with a slope of 0.03 m/m. It has a drainage area of 40 km^2 and elevations range between 1,830 and 2,740 m in a montane forest within a confined bedrock valley (Doughty et al., 2020). Seasonal peak flows come predominantly from snowmelt with groundwater and summer rainfall as secondary inputs. Previous research suggests that the presence of instream wood in multiple reaches of Little Beaver Creek enhances solute retention and does so more than the changes in channel morphology associated with instream large wood (Ader et al., 2021). We selected two reaches for tracer injections and ER imaging, each with at least one channel-spanning logjam that remained stable from year to year based on field observations (Figure 2). Reach characteristics are summarized in Table 1.

Reach 1 is upstream and is the more complex reach of the two in this study (Figures 1 and 2a-2c). The valley-bottom width is approximately 26-m wide (looking upstream, measured from the leftmost to the rightmost bank of active channel width), and is a multi-channel, multi-jam reach with two channel-spanning logjams. The primary channel has an average bankfull channel width of 9 m at the upstream ER transect, below which the channel is divided in two, with a channel-spanning logjam at the head of each branch. The primary (southern) channel contains surface flow at all discharges, while the secondary (northern) channel exhibits surface flow at medium and high discharge. A fallen tree stabilizes the logjam on the primary channel (Figures S1–S3 in Supporting Information S1), and several fallen branches from nearby vegetation stabilize the logjam on the secondary channel. Both logjams in Reach 1 have a collection of entrapped woody material of varying size that form the bulk of each logjam. The logjams in Reach 1 were beaver-modified and appeared to be less porous than the logjam in Reach 2, described below. In Reach 1, the logjams create a backwater pool in the channels upstream of each logjam (Table S1a in Supporting Information S1) that contain small to large woody material and sandy deposits that extend about 5 m upstream (Figures S1 and S2 in Supporting Information S1). Two channels flow upstream of the logjams along the south and north side of the valley (Figures 2a–2c). The secondary channel enters the

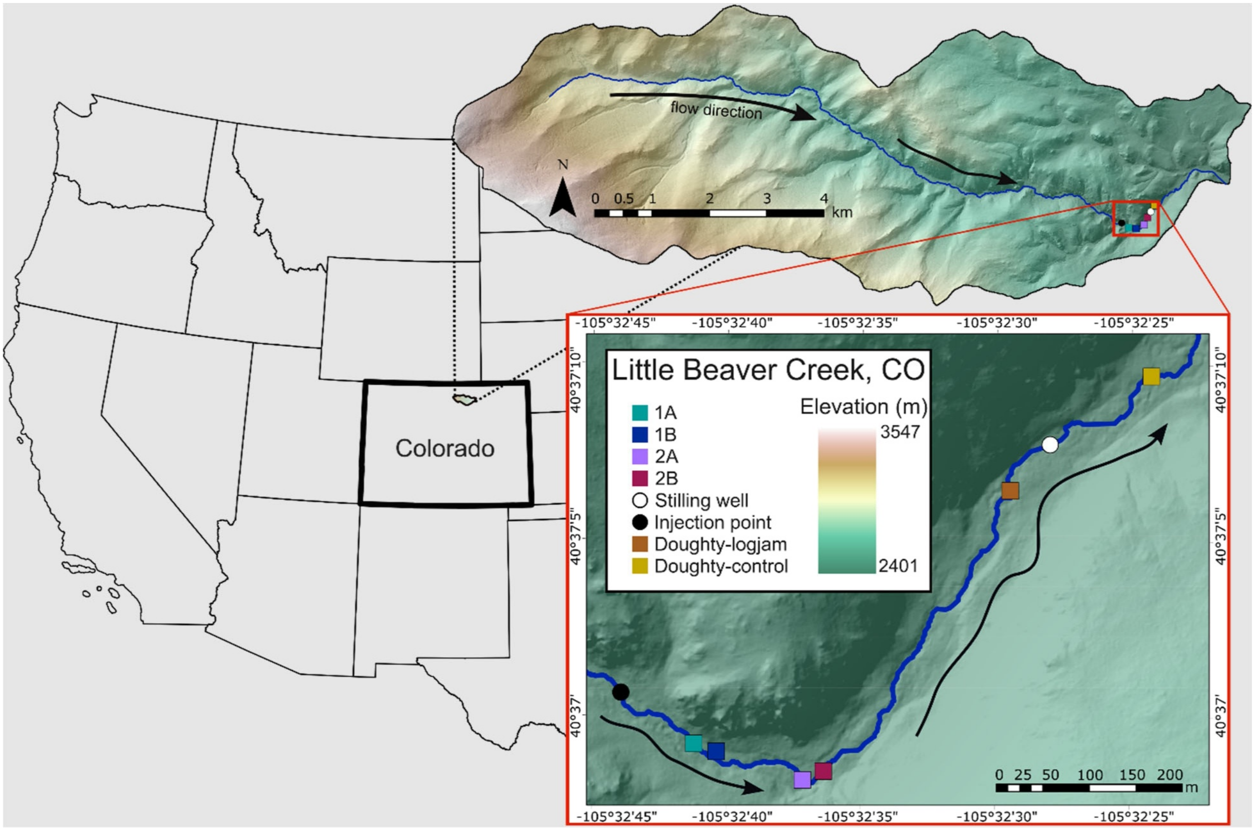

Figure 1. Study site at Little Beaver Creek, Colorado. The upstream reach, Reach 1, consists of electrode transects 1A and 1B for electrical resistivity (ER) measurements where A is the upstream transect and B is the downstream transect. The downstream reach, Reach 2, consists of electrode transects 2A and 2B, where A is again the upstream transect and B is the downstream transect. Black arrows indicate the direction of flow. Discharge measurements were conducted near the stilling well (white circle). The two sites described in Doughty et al. (2020) are also shown for reference.

primary logjam's backwater pool and turns 90°, flowing perpendicular to the valley wall (Figure S1 in Supporting Information S1; Figures 2a–2c). Flow from the secondary channel continues perpendicular to the valley wall until it recombines with the primary channel as it enters the backwater pool of the southern logjam. Downstream of Reach 1 the stream continues as two channels that are parallel to the valley walls (Figures 2a–2c). These channels bracket a floodplain that consists of organic sandy soil, woody material, and dense vegetation. During high discharge, rills formed on the floodplain flow from south to northwest and join the secondary downstream channel.

The comparatively less complex downstream reach, Reach 2, has a valley-bottom width of approximately 24 m and an average bankfull width of 7.5 m above its single channel-spanning logjam (Figures 2d–2f). The bulk of the logjam consists of a single fallen tree, which has amassed smaller woody material (Figures S4 and S5 in Supporting Information S1). Downstream of the logjam, the creek divides into two channels that contain flow at all discharges (Figures 2d–2f; Figure S5 in Supporting Information S1). Below the logjam, the valley-bottom width narrows to approximately 19 m. The channels are divided by an island that extends about 10–15 m downstream and ends where the channels rejoin (Figure S5 in Supporting Information S1). The southern bank is highly eroded near the logjam, ~1-m tall and steep (nearly 90°), and is sparsely vegetated, except for several trees with roots that appear to stabilize portions of it (Figure S4 in Supporting Information S1). Erosion has created a secondary channel about 0.5 m wide between the bank and the southern side of the logjam where a small portion of the stream flows (Figure S4 in Supporting Information S1). The north bank and the floodplain of the creek are highly vegetated, with grasses and a stand of willows that extend into the stream channel (Figure S4 in Supporting Information S1). The logjam creates a large backwater pool that saturates the low-lying banks upstream and has captured a considerable amount of sandy sediment and woody material (Table S1b; Figure S4 in Supporting

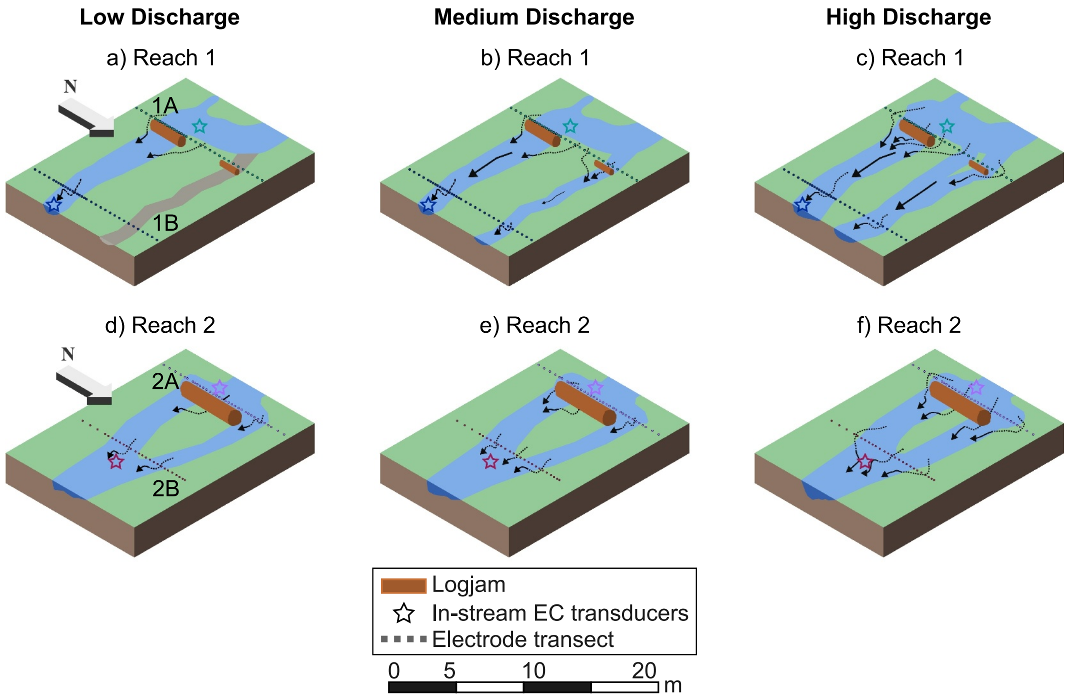

Figure 2. Schematics of Reach 1 (top row) and Reach 2 (bottom row) at low, medium, and high discharge from left to right, respectively. Flow is west to east, or top to bottom in these images. Arrows represent flow vectors where solid segments indicate instream flow and dotted segments indicate subsurface flow. There is no surface flow in the secondary channel of Reach 1 at low discharge (colored gray in a). The location of electrical resistivity observation transects (dotted lines), and in-stream electrical conductivity transducers (stars) are shown. Electrode transects are denoted by the reach number followed by A for the upstream transect or B for the downstream transect within each reach. Backwater pools are shown schematically above the logjams where present.

Table 1
Summary of Reach Characteristics (Some Data Reproduced From Ader et al. (2021)) and Electrical Resistivity Measurements in Those Reaches

Characteristic	Reach 1	Reach 2
Channel gradient (m/m)	0.034	0.029
Bankfull channel average depth (m)	0.60	0.53
Bankfull channel average width (m)	9	7.5
Valley-bottom width at ER transects (m)	26	24
Number of logjams	2	1
*D*50 (mm)	60	45
Wood load (m^3/ha of channel surface)	110	360
Proportion of wood load in jams (by volume)	0.88	0.94
Average [standard deviation] of jam volume (m^3); volume (porosity) of instrumented jam	4.9 [6.8]; 9.7 (40%)	0.8 [1.6]; 4.3 (60%)
Unit pool volume (m^3/ha of channel surface)	1,120	330
Distance between ER transects (m)	∼30–40	∼15–20
Electrical resistivity line lengths	A: 26.5, B: 26 m	A: 23.9, B: 19.2 m
# of electrodes in transects	A & B: 34	A: 34, B: 26

Note. The distance between Reach 1 and Reach 2 is ∼190 m. The tracer mixing length from the injection location to the top of Reach 1 is ∼100 m.

Table 2
Details of the Tracer Tests

	Stream discharge (m^3/s)	Background stream EC (μS/cm)	Tracer injection rate (m^3/s)	Mean tracer EC (μS/cm)	Total mass of tracer injected (kg)
04/6/19	0.5	36.6	5×10^{-5}	245	204
24/6/19	1.1	23.1	9×10^{-4}	235	356
12/8/19	0.2	28.0	4×10^{-5}	244	153

Note. Note that the tracer EC varied slightly throughout the test as multiple containers were mixed with NaCl throughout the injection, rather than one, single tank. The EC in column 5 is that of the injectate, not the EC of the stream once the tracer was introduced.

Information S1). Standing water can be seen within the soils of the low banks along the backwater pool, especially on its southwestern edge.

2.2. Tracer Tests

Three tracer tests were completed at different stream discharges (Q) to observe the influence of discharge on solute transport in the experimental reaches and are summarized in Table 2. The tracer tests were conducted on 4 June 2019, at $Q = 0.5$ m^3/s (before peak snowmelt), 24 June 2019, at $Q = 1$ m^3/s (just after peak snowmelt), and 12 August 2019, at $Q = 0.2$ m^3/s, (baseflow conditions) (Figure 3). Discharge was estimated from velocity measurements using a FH950 Handheld Flow Meter at 20–25 cm intervals across the stream. The discharge measurements were completed at the stilling well, downstream of our reaches (Figure 1). Discharge measurements from June 2018 to July 2020 were used to develop a rating curve (Figure S6 in Supporting Information S1).

A tracer created from NaCl dissolved in stream water was injected approximately 100 m upstream of Reach 1 (Figure 1) to ensure adequate mixing of the tracer with the stream (González-Pinzón et al., 2022). Because dissolved cations and anions are electrically conductive, we can detect increases in Na^+ and Cl^- concentrations from instream EC loggers and characterize the tracer migration in the subsurface with ER surveys. The dissolved NaCl injection rate and concentration were designed to raise the stream water EC by at least 50 μS/cm for each of the three tracer tests, leading to different injected masses depending on discharge, and the tracer was injected at a constant rate for 4 hr. HOBO Fresh Water Conductivity Data Loggers (HOBO U24)—co-located with ER electrode transects described below—were used to record instream EC upstream and downstream of each logjam in both experimental reaches (Figure 2). Additionally, an EC logger was installed above the injection site to record background EC (Figure 1). These EC loggers were set to record observations every 60 s (~0.02 hr), starting an hour before tracer injection began and continuing more than 24 hr after the end of injection to ensure that EC

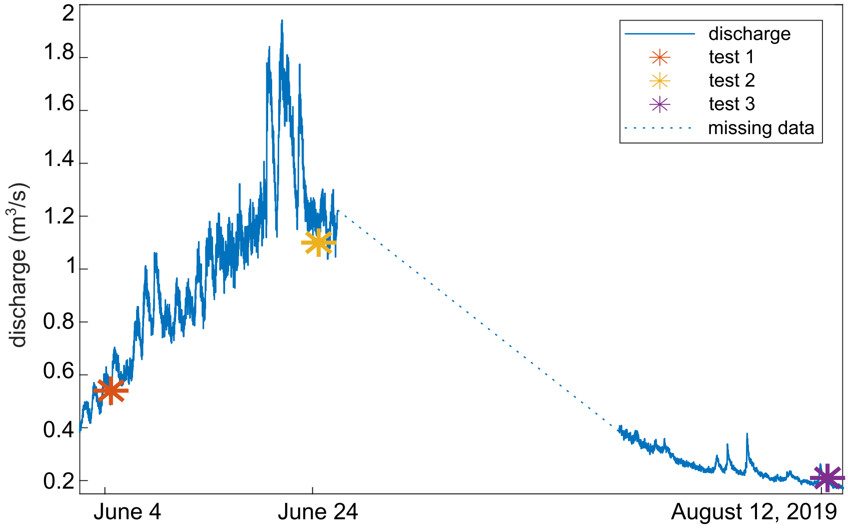

Figure 3. Hydrograph generated from stage calculations and rating curve (Figure S6 in Supporting Information S1), showing estimated discharge during the timespan of the three tracer tests. The data gap is due to equipment failure between site visits.

returned to background or near-background levels (within 1% of background EC). Instream EC values were corrected for changes in temperature assuming a linear relationship between EC and temperature (Keller & Frischknecht, 1966). We note that the secondary channels were not instrumented with EC loggers (although they were straddled by the ER electrode line). Instead, EC measurements were made below the merger of the two flowing channels in Reach 2 to capture tracer transport through both channels and in the main channel of Reach 1, partially because the secondary channel was quite shallow during the first experiment. We consistently placed the loggers at the same locations for all experiments (Figure 2).

2.3. Electrical Resistivity Data Collection

An IRIS Syscal Pro Resistivity Meter was used to measure electrical resistivity of the subsurface near the logjams. The resistivity meter introduces a low-frequency alternating current across a pair of electrodes and the resultant voltage is measured between another pair of electrodes, which represents a bulk response to the rock type, pore size, water saturation, surface charge, total dissolved solids, and temperature (e.g., Keller & Frischknecht, 1966). The four electrodes used in each measurement are called a quadrupole and electrical resistivity data were collected using a dipole-dipole geometry for speed of data collection (Binley & Kemna, 2005).

Four transects were monitored throughout each of the three tracer tests (Figure 2; details in Table 1). Each transect consisted of electrode lines that were installed into the banks and streambed. When the water level was high, electrodes were floated at the water surface, rather than installed into the bed. Electrode spacing was 0.5 m throughout the stream expanding to 1 m on the banks. Each electrode line spanned ~3 m from the edge of each bank plus the width of both channels in a reach. Electrode lines consisted of 34 electrodes (transects 1A, 1B, and 2A) or 26 electrodes (transect 2B), depending on the width of the reach. Total line lengths were 26.5, 26, 23.9, and 19.2 m, respectively, moving from upstream (1A) to downstream (2B). Five hundred and nineteen quadrupoles were collected per time step for all 34-electrode transects, and 277 quadrupoles were collected for the transect with 26 electrodes. Two stacks (i.e., duplicate measurements) were collected per quadrupole; stacking errors were reported as the coefficient of variation of those stacks in percent, where the mean stacking error was ~1% and the median was ~0.3% (Table S2 in Supporting Information S1). It took 20–30 min (0.3–0.5 hr) to collect these measurements per timestep. Background ER data were collected along the transects for a minimum of 1 hr before the injection began. Data collection continued during the 4-hr injection and for a minimum of 26 hr after the injection ended for each tracer test.

Apparent bulk EC (σ_{ba}) [μS/cm] was calculated from the ER data using Ohm's Law:

$$\sigma_{\mathrm{ba}} = \frac{I}{\mathrm{VK}} \tag{1}$$

where I is the injected current (amperes), V is voltage (volts), and K is the geometric factor (m), which accounts for the arrangement of the electrodes:

$$K = \frac{2\pi}{\frac{1}{\overline{\mathrm{AM}}} - \frac{1}{\overline{\mathrm{AN}}} - \frac{1}{\overline{\mathrm{BM}}} + \frac{1}{\overline{\mathrm{BN}}}} \tag{2}$$

where A and B are the two injection current electrodes, M and N are the potential electrodes and $\overline{\mathrm{AM}}$, for example, is the distance between the current electrode A and potential electrode M where the overbar indicates the distance between respective current and potential electrodes. By averaging the σ_{ba} values from all quadrupoles each timestep, a composite σ_{ba} BTC for each ER transect over time was generated. These resultant σ_{ba} BTCs, which have a measurement support volume that is difficult to quantify because it is dependent on the electrical conductivity of the earth (e.g., Singha & Gorelick, 2006), were then compared to instream EC BTCs, which measure EC values at a point. Because ER methods are sensitive to temperature (Hayley et al., 2007, 2010), temperature data were collected just upstream of transects 1A and 2A at 10 and 40 cm depth within the streambed using iButton temperature probes that measured every 10 min (0.17 hr). Daily temperature variations were quite small, with the largest value (1.2°C) occurring at Reach 1 at a depth of 10 cm. Therefore, σ_{ba} values were not temperature corrected for the time-lapse inversions at each of the three data-collection times, which were inverted independently such that temperature changes between data-collection times did not matter. Additionally, because observation times varied between each tracer test, breakthrough curves were truncated at 30 hr to maintain consistent time scales across all three tracer tests and to preserve most of the data for the quantitative comparisons described below.

2.4. Temporal Moments, the Transient Storage Index, and Residence Time Distributions

There are multiple methods commonly used in tracer transport studies to quantify processes from BTCs. Here, we calculated temporal moments, the transient storage index, and residence time distributions, as are frequently done in other stream studies. We outline these three methods in brief, with more details available in Supporting Information S1.

First, tracer concentration was estimated from observed instream and σ_{ba} EC by assuming a linear relation between EC and concentration of total dissolved ionic solids (Keller & Frischknecht, 1966). To find this relation, our tracer injectate was diluted to different concentrations in the lab and compared with the resulting measured EC such that the following relation was found with an R^2 of 0.99:

$$C = 0.3\mathrm{EC} \tag{3}$$

where EC was in μS/cm and C is in mg/L.

Once the data were converted to concentration, we calculated temporal moments (e.g., Gupta & Cvetkovic, 2000; Harvey & Gorelick, 1995)

$$M_n = \int_0^t t^n C(t)\,dt \tag{4}$$

where M_n is the nth temporal moment, t is time, C is stream concentration. For these experiments, the chosen end time was 30 hr (26 hr after the tracer injection ended) to keep observation times consistent across all tracer tests and observation transects. These moments provide information on the tracer mass passing the measurement point, the mean arrival time (related to advection), temporal variance (related to dispersion and diffusion), and skewness (a function of retention). Asymmetry in breakthrough curves is interpreted as a proxy for solute retention in a system (Ward et al., 2010a, 2010b). A higher positive skewness indicates longer tracer retention times and HEF. Higher-order moments such as kurtosis can also be calculated from BTCs. One important limitation of temporal moments is their dependence on the tail of the concentration data, which can be noisy or truncated in experimental studies (e.g., Young & Ball, 2000). The equations used here, and in most stream hydrology studies, also assume a single mode/peak in the concentration BTCs, which may oversimplify complexities observed in natural systems.

Other methods beyond moments exist to explore retention, including the transient storage index (TSI), a metric that may minimize the impact of problematic or truncated tails (Mason et al., 2012):

$$\mathrm{TSI} = t_{99} - t_{\mathrm{peak}} \tag{5}$$

where t_{99} is the time it takes for 99% of the tracer to move through the observation point and t_{peak} is the time elapsed between the start of the tracer injection and the peak concentration of the BTC. The TSI compares transient storage, reflected by the amount of information stored in the tail of the BTC, against advective transport conveyed by the amount of information in the peak of the BTC (e.g., Harvey et al., 1996; Mason et al., 2012). To enable comparisons across different discharges and reaches, we used normalized TSI (after Gooseff et al., 2007):

$$\mathrm{TSI}_{\mathrm{norm}} = \frac{\mathrm{TSI}}{t_{\mathrm{peak}}}. \tag{6}$$

This normalization allows us to characterize transport processes consistently, independent of discharge magnitude or spatial context (Ward et al., 2013).

Temporal moments are proportional to the reach length divided by the velocity, and also strongly affected by the retention processes occurring along the reach. Consequently, to assess the responses of individual reaches, we used deconvolution methods to assess the distribution of travel times between upstream and downstream BTCs. As discussed by Cirpka et al. (2007), Payn et al. (2008), and Gooseff et al. (2011), the equations of solute transport and mass transfer between the stream and shallow groundwater (i.e., hyporheic zone) may be written as a simple convolution, if and only if the equations are linear and time-invariant. In that case,

$$C_{\text{out}}(t) = \int_0^t g(\tau)\, C_{\text{in}}(t-\tau)\, d\tau, \tag{7}$$

where $C_{\text{out}}(t)$ is the downstream concentration, $C_{\text{in}}(t)$ is the upstream concentration, and $g(t)$ is a non-negative transfer function of total travel times between the locations. If the observation time far exceeds the mean residence time in an immobile (e.g., hyporheic flowpath) phase, then all mass should be recovered in the mobile (stream) phase. Then this function is a probability density function (that is, mass is conserved in the mobile phase when $\int g(t)\, dt = 1$).

2.5. Inversion of Electrical Resistivity Data

To visualize tracer transport and retention in the subsurface, the σ_{ba} data were also inverted using ResIPy (Blanchy et al., 2020), which is based on the well-established code R2 (e.g., Binley & Kemna, 2005). R2 is an inverse model based on Occam's solution that accounts for 3-D current flow (Binley & Kemna, 2005). Given our observed σ_{ba} data collected from the ER surveys, the code solves a regularized optimization problem such that the resulting model explains our observations while minimizing an objective function, parameterizing the subsurface in terms of “actual” rather than apparent bulk electrical conductivity (Binley & Kemna, 2005). R2 is a finite-element-based code that allows for topography and modeling of bounded regions and uses a weighted least-squares function coupled with several regularization options. We used the time-lapse survey capability, which calculates the percent difference from background data so that errors related to model discretization and field configuration are minimized (LaBrecque & Yang, 2001). After topographical data are imported, ResIPy uses Gmsh (Geuzaine & Remacle, 2009) to generate an irregular triangular mesh that is finer near the electrodes, and encompassed by a coarser mesh that extends to greater lateral distance and depth. Domain boundaries were defined as zero-flux, as is commonly assumed in electrical flow modeling, and were placed ∼130 m beyond the endpoints of each ER transect. The resolution matrix R was calculated to show how well each parameter is resolved in each iteration of the inversion (e.g., Binley & Kemna, 2005):

$$R = \left(J_{\text{k}}^{\text{T}}\, W_{\text{d}}^{\text{T}}\, W_{\text{d}}\, \text{J}_{\text{k}} + \alpha W_{\text{m}}^{\text{T}} W_{\text{m}}\right)^{-1} J_{\text{k}}^{\text{T}}\, W_{\text{d}}^{\text{T}}\, W_{\text{d}}\, J_{\text{k}} \tag{8}$$

where J is the Jacobian (sensitivity) matrix, T is the transpose operator, k is the final inversion iteration, W_{d} is a data-weighting matrix associated with individual data errors, W_{m} is the model weighting matrix, and α is the regularization parameter. Values on the diagonal of R equal to one indicate that the parameter was perfectly resolved. Values near zero specify parameters that cannot be uniquely resolved. Generally, resolution decreases with depth and distance from the electrodes (Day-Lewis et al., 2005). We also estimated the depth of investigation (Oldenburg & Li, 1999), where two inversions were run for a time step with two different homogeneous starting models. The ratio of the difference in the subsequent inversions gives an estimate of the depth-of-investigation (Blanchy et al., 2020), providing a metric for assessing which model parameters are poorly constrained by the data (Oldenburg & Li, 1999). We do not interpret changes below the depth of investigation as meaningful.

3. Results and Discussion

3.1. Instream EC Breakthrough Curves

During each of the three tracer tests, we observed similar trends in the instream EC BTCs in both study reaches; specifically, a rapid rise in instream EC shortly after beginning the injection, followed by an imperfect plateau due to slight differences in tracer mixing between containers, and a quick return to background or near-background levels after the injection ends (Figure 4). The terms “low”, “medium”, and “high” are used to refer to the corresponding stream discharge levels of the tracer tests, that is, 0.2, 0.5, and 1.0 m^3/s, respectively. Unsurprisingly, at all discharges, tracer breakthrough (i.e., the initial detection of the tracer, defined as EC > 5% of the maximum calculated instream EC at that transect, based on the reported accuracy of the HOBO U24) occurred earliest at the

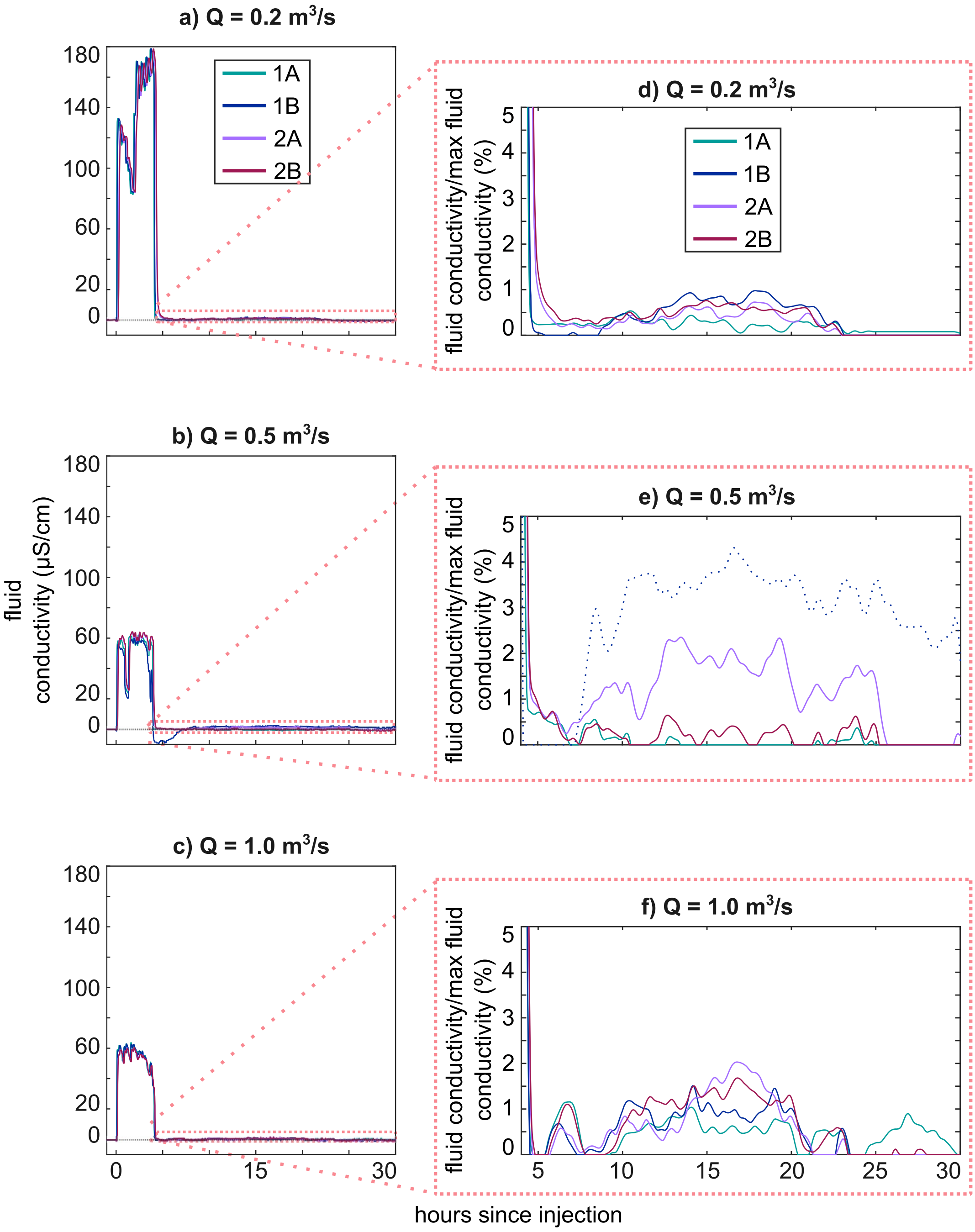

Figure 4. Instream electrical conductivity BTCs with background levels removed for all four transects and three discharges: (a) 0.1 m^3/s, (b) 0.5 m^3/s and (c) 1 m^3/s. The distance between Reach 1 and Reach 2 is approximately 190 m. Instream BTCs across all tracer tests remain above background EC levels throughout the test interval, except for the $Q = 0.5$ m^3/s tracer test. During the 0.5 m^3/s tracer test, the EC transducer in 1B was exposed to air, which is illustrated by the negative values in the tail from 4 to 7 hr of its breakthrough curve (b) so is dotted in (e). Note variability in the plateau concentration as a function of multiple tracer containers being mixed and injected throughout the test. (d–f) Zoomed in plots of the BTCs in a–c as denoted by the red dotted rectangle, smoothed using a 61-point Hanning window and standardized by the maximum instream EC of each transect for visual comparison. The negative excursion in the tail of the Transect 1B curve at 0.5 m^3/s was corrected using trends from the associated BTCs from the surrounding transects during the same tracer test (see Text S1 in Supporting Information S1).

most upstream transect (1A) and latest at the most downstream transect (2B; Figure 4; Table S3 in Supporting Information S1). At all discharges, tracer breakthrough at 1A occurred ~3 min (0.05 hr) after injection began, similar values within noise given a short transport distance. The breakthrough time at transect 2B decreased with increasing discharge and occurred ~16 min (0.27 hr) after injection at low discharge, ~10 min (0.17 hr) after injection at medium discharge, and ∼8 min (0.14 hr) high discharge. During the low- and medium-discharge tracer tests, there is a brief, rapid decrease in EC after beginning the injection due to temporary clogs in the injection tube at 35–40 min (0.58–0.67 hr) (Figures 4a and 4b). The magnitude of EC was higher in the stream during the low-discharge tracer test compared to the medium and high discharge tracer tests due to less dilution. These variations in concentration manifest as differences in calculated mass in the temporal moments, described below (Text SI, Section S1 and Table S4 in Supporting Information S1).

There is a small second peak in the late-time tails of the BTCs in all three tracer tests, in both reaches (Figures 4d–4f), with a magnitude near the logger resolution. (Note that the data in transect 1B, at medium discharge, were largely disregarded due to the EC logger being exposed to air near the end of injection (Figure 4b). We keep these data in Figure 4e for completeness, given small sample sizes, but show them as a dotted line.) It is striking that the secondary peaks are largely consistent, in timing and magnitude, across experiments and regardless of location within the system, although they are smaller at low discharge (Figures 4e and 4f). While these secondary peaks are small in terms of absolute magnitude or percent change in electrical conductivity, the consistency of their occurrence in the data between reaches and discharges suggests a system-wide phenomenon rather than spurious effects. It is possible that these secondary peaks are a function of solute retention in backwater pools. As discharge increases, we observe expanding width and depth of the backwater pools located upstream of transects 1A and 2A (Table S1 in Supporting Information S1); similar results were simulated in Zhang et al. (n.d.). The physical expansion of these backwater pools provides additional volume that could increase temporary retention of surface water and solutes. This increase in storage may manifest in the BTCs as a temporal spreading of the tracer signal, potentially driving delayed secondary peaks indicating the release of tracer from storage zones at later times as seen at this site in Doughty et al. (2020), as well as other sites where eddy rotation was hypothesized to lead to periodicity of tracer signals (Gooseff et al., 2011). Because eddy rotation cannot be simulated in HydroGeoSphere, this hypothesis could not be tested by Zhang et al. (n.d.). Either way, these late-time peaks affect our ability to meaningfully use moment analyses that assume a single mode, as is discussed below and Text S1.1 in Supporting Information S1.

In the absence of storage, the time it takes for the instream EC to return to background levels is expected to be inversely correlate with discharge as higher discharge typically translates to faster stream velocity, and breakthrough time generally decreases with increasing discharge in both reaches. However, the fastest return to background occurred at medium discharge in Reach 1, although the differences are small and the signal-to-noise ratio is low (EC returned to background levels at ∼0.2, 0.04, and 0.1 hr after the end of injection at low, medium, and high discharge, respectively; Figures 4d–4f). If significant, the differences here may be controlled by the secondary channel that formed in Reach 1 between low and medium discharge tracer tests. The secondary channel was smaller than the primary channel and had visibly slower flow velocities based on observed movement of debris on the water surface. At medium discharge, when the secondary channel was active in Reach 1, there are shallower flowpaths than at higher flow (as supported by the ER inversions, below). At high discharge, higher stream stage may have generated steeper pressure gradients, driving more downwelling and subsurface exchange into the banks, resulting in slower flushing of the tracer when compared to medium discharge, leading to the faster flushing and quicker return to background at medium discharge. This hypothesis is supported by the numerical models of Zhang et al. (n.d.). In Reach 2, it took approximately 0.6 hr at low discharge and 0.2 hr after the end of injection at medium and high discharge to return to background conditions (Figures 4d–4f).

3.2. Bulk EC (σ_{ba}) Breakthrough Curves

Trends observed in σ_{ba} BTCs resemble those observed in the instream EC BTCs (Figure 5): σ_{ba} shows a rapid increase, followed by a variable plateau that mimics the instream EC, a subsequent decline toward near-background levels, and then a smaller, secondary peak (Figures 5d–5f). In this case, however, the secondary peak often exceeds 1% of the maximum measured σ_{ba} in that transect, which is notably larger than noise. We once again observed the earliest change in σ_{ba} at upstream transect 1A and the latest at downstream transect 2B, as would be expected.

Despite some similarities, there are also notable differences between the σ_{ba} BTCs and those of the instream EC, including in timing. The most notable difference is that after the plateau, the decline in σ_{ba} is much slower than that of the instream EC, evidenced by the long and gradual tail in the receding limb (Figure 5). Because σ_{ba} measurements encompass a larger support volume than that of the instream EC measurements and are sensitive to

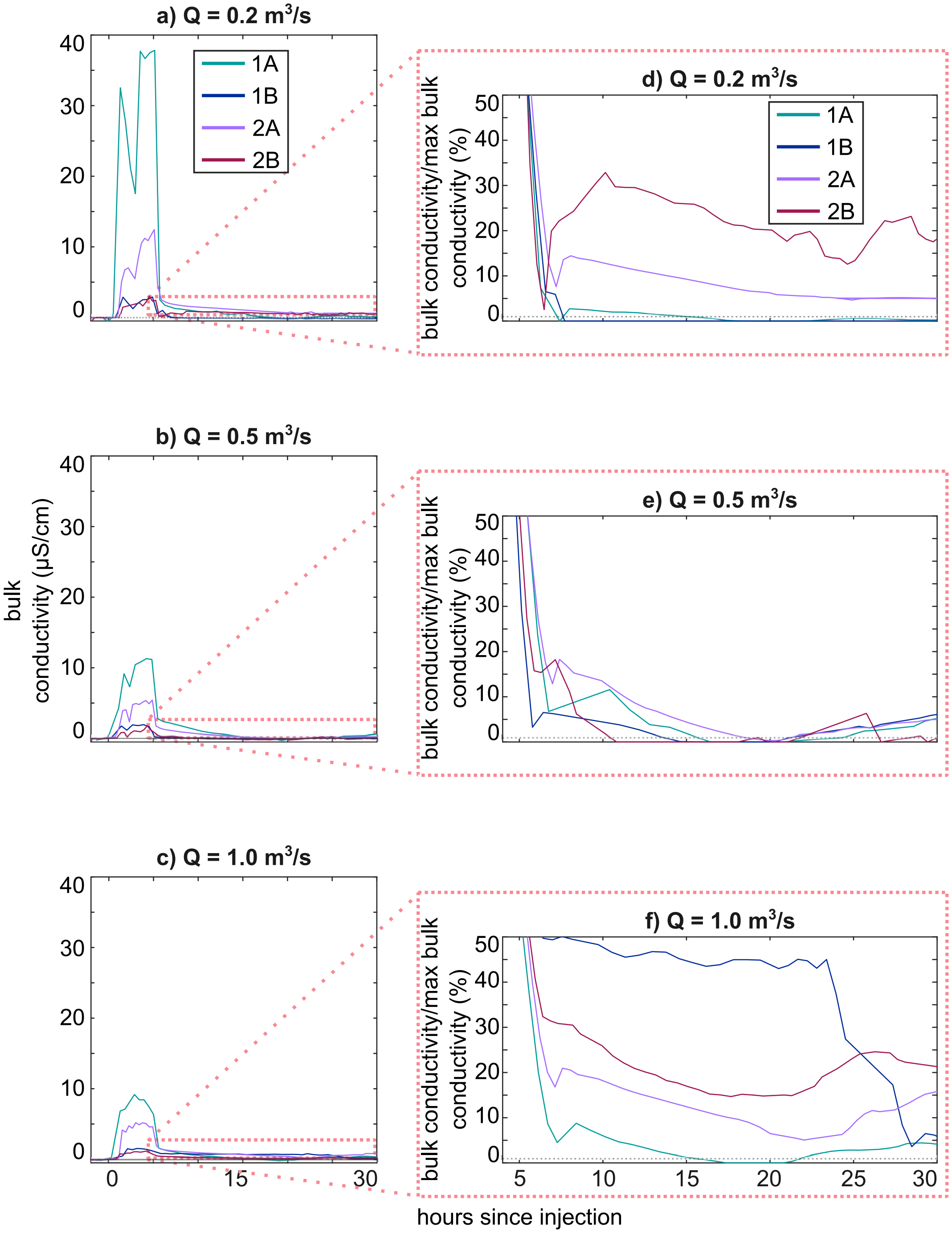

Figure 5. Bulk electrical conductivity (σ_{ba}) BTCs with background levels removed for all four ER transects at three discharges: (a) 0.1 m^3/s, (b) 0.5 m^3/s and (c) 1 m^3/s. (d–f) σ_{ba} BTCs standardized by maximum bulk EC of each transect and smoothed using Savitzky-Golay filter with a 0.25 smoothing factor. Percent change magnitudes in σ_{ba} BTCs are an order of magnitude larger than instream EC BTCs.

changes within the aquifer as well as the stream, σ_{ba} BTCs are inherently slower to return to background conditions than EC values within the stream. Similarly, σ_{ba} BTCs generally show later mean arrival times than the instream BTCs across all discharges (Tables S4 and S5 in Supporting Information S1), which, again, is likely a function of the larger support volume of the ER measurements compared to that of the EC loggers as well as their extended tails. Also, few of the σ_{ba} data completely returned to background levels at any discharge (Figure 5).

While noisy, the presence of secondary peaks suggests notable subsurface solute retention, which is greatest at high discharge; this result becomes clearer upon inversion of the σ_{ba} data (described below).

Another difference between the σ_{ba} BTCs and those of the instream EC is the magnitude of the conductivities. The conductivity magnitudes of σ_{ba} are smaller than that in the instream EC BTCs throughout all tracer tests, as expected, because σ_{ba} measures the bulk medium, rather than just the surface flow (Figures 4 and 5); consequently, the estimated mass from the σ_{ba} BTCs is much smaller than that estimated from the instream EC (details in Tables S4 and S5 of Supporting Information S1). Also, the magnitude of response varies more between transects for σ_{ba} than those of the instream EC BTCs (Figures 4a–4c and 5a–5c). For each discharge, the σ_{ba} values show systematic decreases between A and B transects (i.e., above/below logjam(s)) in each reach) and between 1A and 2A transects (above logjam(s)) between reaches), while 1B and 2B values (below logjam(s)) are similar between reaches (Figure 5). In contrast, the EC values are similar across all transects for a given flow (Figure 4). The averaging over large support volumes with ER limits the accuracy of mass recovery in highly concentrated targets (i.e., measurement of conductivity in streams that are channelized like those of transect 1B and 2B) but may allow for better assessments of more distributed tracer presence like in 1A and 2A (e.g., Bethune et al., 2015; Ward et al., 2010a), meaning that we underestimate masses in systems like 1B and 2B, which may explain the differences in σ_{ba} values downgradient. For example, we see the lowest σ_{ba} (and thus the lowest observed mass and mass recovery; Table S5 in Supporting Information S1) at transect 1B at the lowest discharge, likely due to the target being highly focused, rather than more dispersed at higher discharges.

3.3. ER Inversions

Inversions of the σ_{ba} data provided spatially explicit evidence on how channel morphology and logjams enhance subsurface transport of the tracer. The σ_{ba} data, presented above, were inverted to create maps of the strength and distribution of the ER signal through time that was generated as a response to tracer presence in the subsurface. The ER current distribution as measured in the field is affected by the electrical conductivity distribution upstream and downstream of our electrode transect as the current moves out of that plane (e.g., Bentley & Gharibi, 2004; Vanderborght et al., 2005). σ_{ba} data from each transect are inverted independently from one another in 2-D, assuming that properties of the medium are invariant in the third dimension (i.e., upstream or downstream; Nimmer et al., 2008; Vanderborght et al., 2005).

3.3.1. ER Inversions at Low Discharge

In Reach 1, which has the intermittent secondary stream that is not activated at low discharge (Figure 2a), we see a broad spatial distribution of the tracer in the upstream transect 1A from 4 to 20 m along the transect (Figures 6i, 6m, and 6q), at depths to and below the depth of investigation. These results suggest the spread of the tracer due to the backwater pool just above the ER line (Figure 2a). The concentrated tracer at ∼7 m along the transect in 1A, near the stream location, likely indicates an area of downwelling and HEF (Figures 6i, 6m, and 6q). The tracer continued to generate a strong signal (47% higher than background) 4–5 m along the transect 1 hr after the injection ended (Figure 6u). The tracer signal is no longer detectable approximately 5 hr after the injection ended. The solute refocuses below the logjam, in transect 1B, around the stream (Figures 6j, 6n, 6r and 6v), which we observe at 5–10 m along the transect to the depth of investigation; this isolated, concentrated signal is indicative of tracer movement through and below the single channel in transect 1B (Figure 2a). The tracer signal persists throughout the entirety of the data collection where small sections of the inversion remained above 10% from background bulk EC ∼6 hr after the injection ended.

Multiple areas light up in the subsurface in Reach 2, the downstream reach with two persistent channels (Figure 2d). In transect 2A, ER inversions show spatially distributed tracer presence across the transect from 4 to 17 m to the depth of investigation (Figures 6k, 6o, 6s and 6w), again as a result of the backwater pool. Tracer signal is no longer observable ∼16 hr after the tracer injection ended (Figure S9 in Supporting Information S1). Transect 2B shows two relatively isolated signals at 5–10 and 13–15 m along the transect to the depth of investigation, indicative of the two streams separated by an island at 12–13 m across the transect (Figures 2d, 6l, 6p, 6t and 6x). The tracer signal becomes undetectable ∼17 hr after the injection ended (Figure S10 in Supporting Information S1).

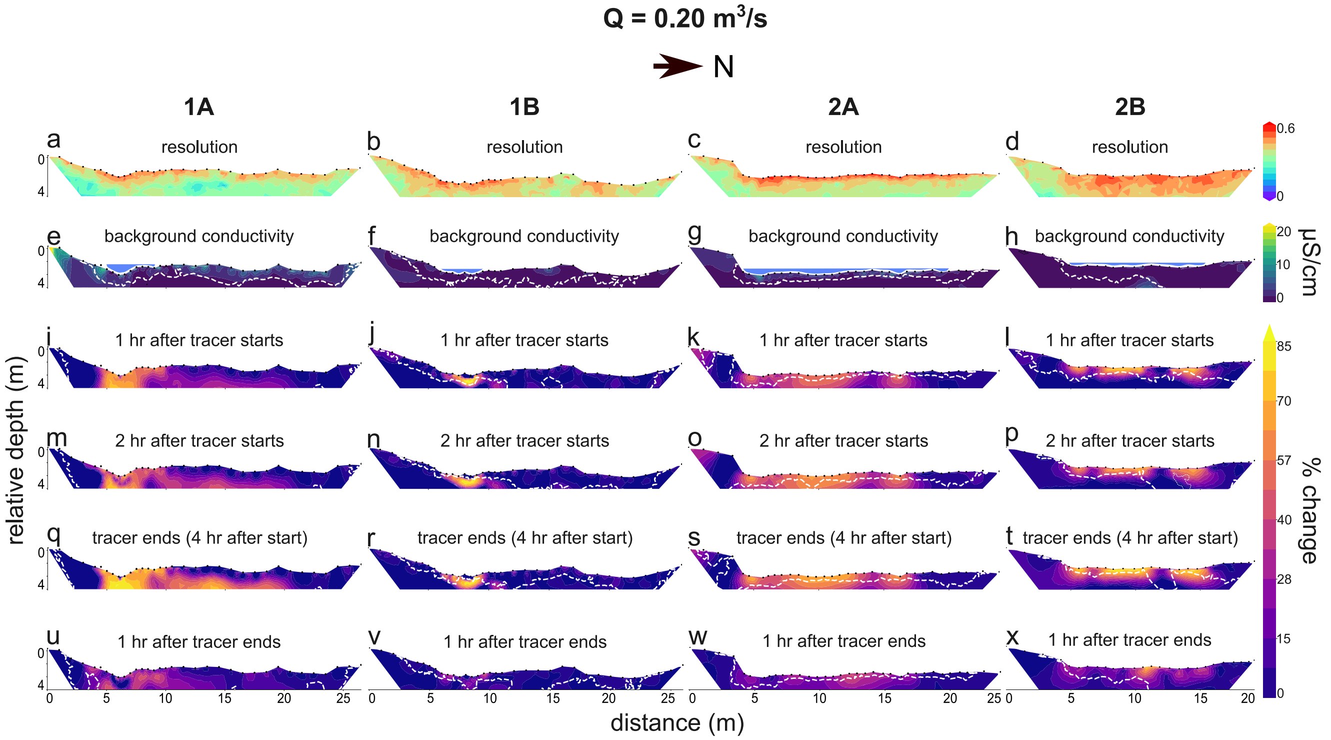

Figure 6. Results from ER inversions across all four transects for selected timesteps from 12 August 2019 (low flow). Cross-sections are oriented looking upstream; flow would be coming out of the page. (a–d) The resolution matrix, where values that are closer to one are more resolved. (e–h) Inverted background bulk EC. Light blue areas on the surface of each transect indicate stream locations (i.e., surface flow). (i–x) ER inversions at 1, 2 and 4 hr after tracer injection began (tracer injection ends at 4 hr), and 1 hr after the tracer injection ends. Percent change represents the percent increase in modeled bulk EC from modeled background EC. White dotted lines represent the depth of investigation, where modeled bulk EC below this line is poorly constrained by observed data.

3.3.2. ER Inversions at Medium Discharge

We observe greater spatial distribution of the tracer in at medium discharge than at low discharge (Figure 7), although perhaps faster flushing. Tracer presence is similar to that observed at low flow along transect 1A, and the signal from the tracer is no longer detectable ~5 hr after the tracer injection ended (Figure S7 in Supporting Information S1). In transect 1B, however, the inversions now show the impact of two channels, the original one at ~7 m (the primary channel) and the now low-flowing secondary channel at 21 m along the transect (Figures 7j, 7n, 7r and 7v). The tracer presence in the secondary channel remains ~14% above background EC ~26 hr after the injection ended. We see similar enhanced subsurface connectivity with discharge in Reach 2. In contrast to low discharge, we observe a less concentrated, but further distributed tracer presence in transect 2A (Figures 7k, 7o, 7s and 7w), particularly in the vicinity of the logjam at 15–21 m. Lateral connectivity at medium discharge (Figures 7l, 7p, 7t and 7x) is similar to low discharge (Figures 6l, 6p, 6t and 6x) in transect 2B, but again appears to flush out of the system more quickly.

The broader spatial extent of the tracer at medium flow is likely driven by multiple changes within the system. As the flow increases to medium discharge, the secondary channel in Reach 1 is activated, and the backwater pools in both reaches expand (Table S1 in Supporting Information S1). These changes, resulting from increased stream stage, drive flow downward into the island (~14 m along transect 2A; Figures 2e, 7k, 7o and 7s) and laterally around the logjams, thereby resulting in the increased vertical and lateral distribution of subsurface flow paths.

3.3.3. ER Inversions at High Discharge

At the highest discharge, we clearly observe the presence of the tracer along the entirety of transect 1A, suggesting a further-expanding hyporheic zone (Figures 8i, 8m, 8q and 8u) that is controlled in part by the growth of the backwater pool (Table S1 in Supporting Information S1), as supported by numerical modeling presented in Zhang et al. (n.d.). Furthermore, the vegetated island that separates the two channels of transect 1A is inundated at high

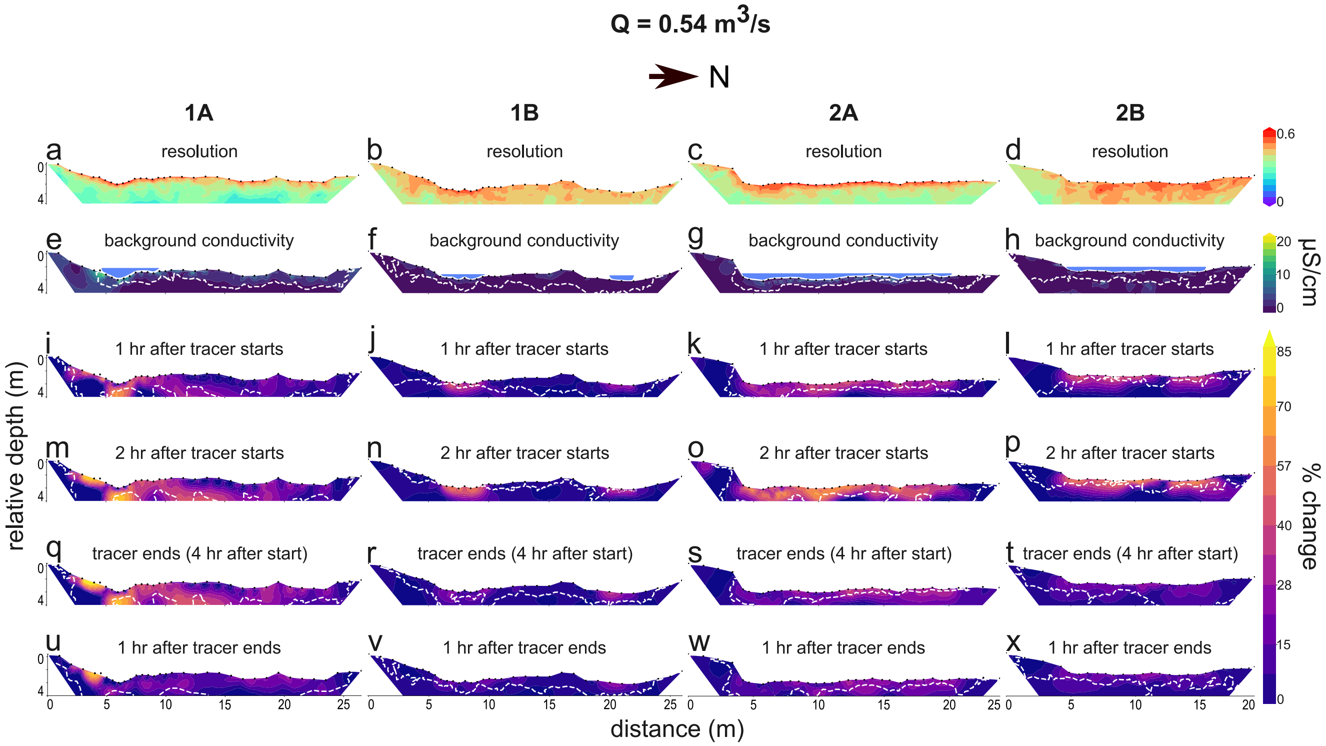

Figure 7. Results from ER inversions across all four transects for selected timesteps from 4 June 2019 (medium flow). Cross-sections are oriented looking upstream; flow would be coming out of the page. (a–d) The resolution matrix, where values that are closer to one are more resolved. (e–h) Inverted background bulk EC. Light blue areas on the surface of each transect indicate stream locations (i.e., surface flow). (i–x) ER inversions at 1, 2, and 4 hr after tracer injection began (tracer injection ends at 4 hr), and 1 hr after the tracer injection ends. Percent change represents the percent increase in modeled bulk EC from modeled background EC. White dotted lines represent the depth of investigation, where modeled bulk EC below this line is poorly constrained by observed data.

flow (Figures 2c, 6–8i, 8m, 8q and 8u; Figures S1 and S2 in Supporting Information S1); this saturated island enhances connectivity across the stream channels and produces highly distributed and nearly unbroken tracer extent across most of the transect (Figures 8i, 8m, 8q and 8u). Only at high discharge is there a second peak in bulk EC in inversions from transect 1A; the tracer signal is undetectable ~8 hr after the injection ended, but the signal returns ~18 hr after the tracer injection ended and remains detectable through the rest of the data collection time (Figure S8 in Supporting Information S1). This delayed second peak is likely caused by enhanced surface transient storage driven by the increasingly large backwater pool coupled to downwelling and subsurface flows. The flowing secondary channel in transect 1B also becomes more apparent in the ER tomography at high discharge, with two relatively concentrated and isolated signals that are representative of the two, well-developed channels at 7 and 21 m along the transect (Figures 8j, 8n, 8r and 8v). The tracer remains detectable through the rest of the observation period.

In transect 2A, the tracer distribution at high discharge resembles that at medium discharge: a highly distributed signal that spreads along the majority of the transect from the increased connectivity and enhanced HEF that is stimulated by the backwater pool in Reach 2 (Figures 2f, 8k, 8o, 8s and 8w; Table S1 in Supporting Information S1). We observe a second peak in bulk EC in transect 2A as well as in transect 1A (Figure S9 in Supporting Information S1). The tracer signal largely dissipates 16 hr after the injection ended but returns 3 hr later (19 hr after injection) and remains detectable 37 hr after the injection ended. In transect 2B, we observe the tracer across the entire width of the transect to the depth of investigation (Figures 8l, 8p, 8t and 8x). Bulk EC in transect 2B remained 5% above background levels throughout the entire data collection, 40 hr after the tracer injection ended, indicating a longer subsurface retention than is seen at medium discharge.

3.4. Discharge-Dependent Patterns of Transient Storage

Increasing stream discharge results in larger backwater pools (Table S1 in Supporting Information S1), the activation of a secondary channel in Reach 1 (Figures 2a–2c), and enhanced subsurface exchange, especially at

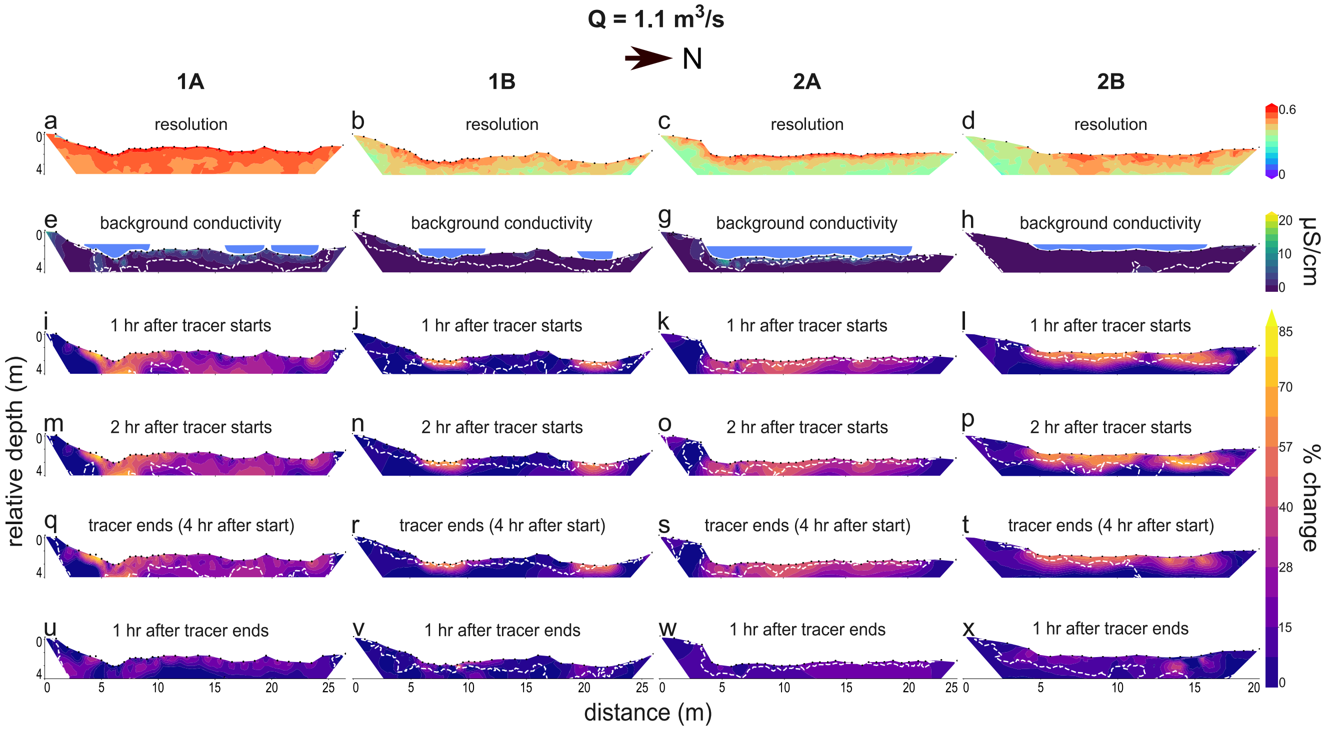

Figure 8. Results from ER inversions across all four transects for selected timesteps from 24 June 2019 (high flow). Cross-sections are oriented looking upstream; flow would be coming out of the page. (a–d) The resolution matrix, where values that are closer to one are more resolved. (e–h) Inverted background bulk EC. Light blue areas on the surface of each transect indicate stream locations (i.e., surface flow). (i–x) ER inversions at 1, 2, and 4 hr after tracer injection began (tracer injection ends at 4 hr), and 1 hr after the tracer injection ends. Percent change represents the percent increase in modeled bulk EC from modeled background EC. White dotted lines represent the depth of investigation, where modeled bulk EC below this line is poorly constrained by observed data.

high flow in transects 1A and 2A, and to a smaller extent in 2B (Figures 6–8). Given the dynamics of our system and noise in our data, the temporal moments and transient storage indices were difficult to explain with respect to physical processes (Tables S4–S6 in Supporting Information S1). There are multiple reasons for this issue, including (a) the changing channel planform, (b) the existence of secondary tracer peaks that complicated the use temporal moments without consideration of multimodal analyses, and (c) noise in the late-time tails of the BTC that made moment analysis difficult, especially for higher-order moments. Analysis of temporal moments and transient storage indices likely work best when the range of tracer concentrations is several orders of magnitude; however, in our case, the signal-to-noise ratio was low, especially in the secondary peaks, as we kept injection concentrations low for both ecological and density-dependent-flow concerns. Consequently, compressing results from these data into single values related to temporal moments and transient storage indices does not make much intuitive sense—in other words, there is a conceptual mismatch between the assumptions needed to interpret breakthrough curves as described in Section 2.4 and the system we are working in.

Despite these concerns, the temporal moments provide some insight into the influence of discharge on transient storage in this system and support some of the ER analyses presented earlier. For example, we see the smallest tracer-mass recovery as well as the highest skew on average, given large values in transects 1B and 2A, occurring at medium discharge (Figure 4, Table S4 in Supporting Information S1). At medium discharge, the secondary channel started to activate in Reach 1 (Figures 2b, 2c, 7j, 7n, 7r and 7v), leading to additional locations for in-stream storage. Stream velocities in the main channel of transect 1B appeared faster than in the secondary channel, thereby promoting variability in advective flowpaths within surface waters at medium flow. This potential increase in the flowpath diversity is also observed in transient storage index (TSI) calculations (Table S6 in Supporting Information S1) and simulated by Zhang et al. (n.d.).

The temporal moments that were calculated from σ_{ba} BTCs, which primarily represent the effects on subsurface transient storage, exhibit a greater range of values at low and high discharge than at medium discharge compared with the instream EC data in both reaches (Figures S11d, S11f and S11h; Table S5 in Supporting Information S1), implying more similarity in subsurface behavior between transects at medium discharge than at other flows. What is most apparent is that the ER inversions show the fastest subsurface flushing of the tracer at medium discharge—that is to say, exchange increases with discharge, based on the extent of tracer in the subsurface, but retention does not.

A more detailed look at the effects of the different reaches on tracer retention and transport may be gained by deconvolving the upstream and downstream signals (Text S3 in Supporting Information S1). The deconvolution gives an estimate of the distribution of total transfer times between upstream and downstream EC time series. These transfer functions were estimated for Reach 1 between transects 1A and 1B (Figure S13 in Supporting Information S1), Reach 2 between transects 2A and 2B, (Figure S14 in Supporting Information S1), and the longer reach between transect 1A and transect 2B (Figure S16 in Supporting Information S1) for both the EC and σ_{ba} BTCs. In short, the deconvolution of the σ_{ba} data and the instream EC data do not indicate a simple mass-transfer process between fast and slow tracer stores (e.g., Gooseff et al., 2011). Neither of the Reach 1 or Reach 2 transfer functions is particularly well-modeled by advection and dispersion, probably because of the short reach lengths. Within Reach 1, the low-flow event showed the greatest retention of tracer mass by single-rate exchange/exponential decay following the main peak, although the medium flow event was corrupted by the downstream electrode failing for a short time. Reach 2 does not show significant retention after the main advection-dominated peak (Figure S14 in Supporting Information S1), while Reach 1 clearly shows larger retention for all flow events. The late secondary peak in upstream 1A is often systematically less than the secondary peaks in downstream sensors, which defies an explanation by either retention or linear transport processes. A small diel rise in the local groundwater concentrations would, however, explain the late-time data. An analysis of all transfer functions indicates that the secondary low-magnitude peaks between 10 and 20 hr are likely due to noise in background EC that varies between locations.

The transfer functions for the longer reach between transects 1A and 2B (Figure S16 in Supporting Information S1) showed a primary peak that was well modeled by pure advection and dispersion, along with the statistically significant secondary peaks that carried minor amounts (<10%) of the total mass. These decline curves of these transfer functions are dominated by multiple peaks at all flows in the short time after removal of the tracer source, rather than monotonic decline as would be expected from mass transfer to/from the hyporheic zone (e.g., Gooseff et al., 2011; Text S3 in Supporting Information S1). These non-monotonic deconvolution results indicate secondary advective pathways, not linear exchange due to concentration gradients. The secondary peaks in the transfer functions could be generated by rotating eddies in the backwater pools or transport through secondary channels, as described earlier. The largest secondary peaks were found during medium discharge, again noting that there is something unusual at medium flow.

3.5. Evaluation of Hypotheses

Our results partially support our first hypothesis. Reach 1, with two logjams and an intermittent secondary channel, exhibits greater variation in advective pathways and transient surface storage than Reach 2, with a single logjam and a perennial side channel. As the intermittent secondary channel in Reach 1 activated with increasing discharge, there was an increase in the number and spatial distribution of flowpaths, including some faster flowpaths that circumvent the backwater storage and lead to faster tracer breakthrough in the channel. The channel complexity and flowpath distribution in Reach 1, with two jams and the intermittent secondary stream, also allows for more interaction between the flowing stream and the subsurface hyporheic zone, leading to an expansion of subsurface tracer signals throughout the transects as seen in the ER inversions (Figures 6–8) and supported by modeling results in Zhang et al. (n.d.). The results from the σ_{ba} and instream EC moments, as well as instream EC and σ_{ba} deconvolutions, suggest that increased reach complexity controls surface transient storage more than subsurface transient storage, which fits previous results from the site (Ader et al., 2021), as well as prior research that observed a linear increase in surface transient storage with increasing wood load (Kaufmann & Faustini, 2012). The higher hydrologic connectivity in Reach 1 facilitates HEF processes, promotes surface retention and the exchange of water and solutes between the surface and subsurface. However, it is difficult to see differences in subsurface retention between the two sites.

Concerning our second hypothesis, our results suggest that transient storage decreases in surface water with increasing flow, but the subsurface patterns are more variable. At higher discharges, the increase in backwater pool volume and, in the case of Reach 1, the activation of the secondary channel, provide opportunities for an

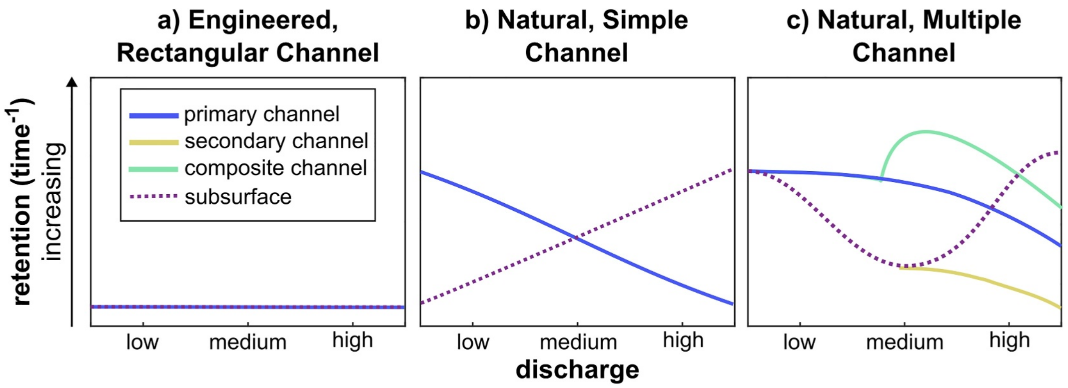

Figure 9. Conceptual figure that shows how surface and subsurface transient storage change with discharge in (a) an engineered, rectangular channel constructed from low-permeability material, (b) a morphologically simple, single-thread, alluvial stream, with no logjams, and (c) a more-complex natural stream with a logjam that develops two channels at medium discharge, as observed in Reach 2 of our study. The magnitudes of the graphs are subjective. The added complexity in (c) likely increases the non-linearity of relations between retention and discharge, although the nature of these relations remains an open question.

increase in overall surface transient storage, although not as a fraction of total flow. While backwater volume increases with discharge, it becomes a smaller portion of the total surface water volume, so total volume may not be an ideal indicator of surface transient storage, but instead relative volume may be more relevant. The secondary stream can in turn drive subsurface exchange flows by increasing the stream stage and associated pressure gradients. The importance of the intermittent secondary stream to surface and subsurface transient storage seems to become less important at high flow, perhaps because dead zones in the surface flow are not as strong with increasing flow, and the increased velocity of the stream allows for less time for exchange of the tracer into the subsurface. Similar patterns in surface transient storage are predicted from the models of Zhang et al. (n.d.) for this site. In the subsurface, we see stronger and more dispersed tracer signals at higher discharge (Figures 6–8), with an increase in the lateral extent of the tracer. Additionally, at low and high discharge, σ_{ba} values remain higher in the tails of the BTCs on average than at medium flow (Figure 5), producing higher subsurface tracer concentrations at later times compared to the medium discharge (Figures 6–8). This result suggests that there is more subsurface solute flushing at medium discharge, which may be related to the deepening of flowpaths in the subsurface (Figures 6–8), but under a lower head gradient than at high flow. We note, however, that high discharge does not always result in a stronger hydraulic gradient between surface water and groundwater (e.g., Wroblicky et al., 1998).

Retention has been defined a number of ways in the literature, but here we lean on the definition of the hydrological retention factor introduced by Runkel (2002), which is the cross-sectional area of the zone of retention divided by the stream discharge. We use this definition because rough estimates of the hyporheic zone cross-sectional area is readily available from our ER mapping. We note that accurate estimates of hyporheic area are impossible from ER data given the effects of regularization on inversion (e.g., Day-Lewis et al., 2005); however, the relative area of the hyporheic zone increases with stream discharge, and discharge increases more quickly than the change in hyporheic area. So while we see an increase in subsurface exchange with discharge, the relation to retention is less clear and, based on flushing, we see the lowest subsurface retention at medium discharge, in contrast to Zhang et al. (n.d.). Of course, differences between our measurements and numerical models are many, in that field measurements are sensitive to aquatic vegetation and complexity in morphology and subsurface heterogeneity that are simplified or absent in simulation. Additionally, surface-water flows are vertically averaged in simulations like those of Zhang et al. (n.d.), so any vertical circulation in the backwater eddies cannot be generated. We note that while many studies have shown that hyporheic flow increases with stream velocity and are is inversely related to retention, Huang and Yang (2023) show a slight decrease in hyporheic flows in a lab system at the highest velocity.

We consequently propose a qualitative conceptual model of how surface and subsurface transient storage (designated here as relative retention, with units of time^{-1}) change with discharge in our field system compared with two simple, hypothetical systems (Figure 9). We note that length and time are required scales to represent the biogeochemically relevant properties of transient storage zones; time determines how quickly the storage is flushed, while length is a measure of the volume per unit bed area in transient storage and controls how easily water can enter the storage zone. One could have high rates of exchange but little storage, for example, in which transient storage would have little or no impact on stream chemistry.

For the simplest stream system, a concrete-lined canal with no hyporheic zone, for example, we would expect little surface and no subsurface retention at all discharges (Figure 9a). We note that several processes may generate some degree of surface retention, however; for example, there may be a viscous sublayer in the turbulent velocity boundary layer near the concrete bottom where water will be stagnant for a time and then flushed back into the water column (e.g., Grant et al., 2018). This viscous sublayer may have little storage; however, the presence of roughness on the concrete might create more substantial storage, especially if there is a benthic algal layer growing there, which may be biogeochemically significant.

In contrast, in a morphologically simple, natural channel surrounded by a permeable aquifer, surface retention might decrease with discharge as increasing stream velocity washes out surface eddies, while subsurface retention increases as more water is driven into slow-moving shallow groundwater (Figure 9b). In this case, the subsurface storage would be large compared to a low-velocity viscous sublayer described above. Additionally, if the hyporheic exchange rate goes up, retention times go down, so such a process would appear more like instantaneous reversible retardation, which cannot be seen in a typical experiment unless a tracer is buoyant. For this simple alluvial channel, we suggest a linear retention model (Figure 9b), but recognize that the relation is likely more complex given stochastic influences of interactions between flow, bedforms, and slight planform irregularities (constrictions, expansions) with varying discharge.

At Little Beaver Creek, no such simple relations exist (Figure 9c). Instead, based on our data, we find that at low discharge in Reach 1, there is substantial subsurface exchange even before activation of the secondary channel (Figures 6–8). As discharge increased to medium flow, activation of the slower-velocity secondary channel increased surface retention and the potential for greater hyporheic exchange through elevated stream stage, as seen in the ER inversions (Figures 6 and 7), but resulted in faster flushing (less retention) of subsurface solute. The ER data further indicate an increase in subsurface transient storage at high discharge, and slower flushing of solute than at medium flow. At high discharge, flow velocities in the secondary channel became more similar to the primary channel than at medium discharge, thereby decreasing flow heterogeneities between the two channels, and perhaps reducing surface retention.

3.6. Limitations of the Study

Although our study compared reaches with varying morphologic heterogeneity that evolved with discharge, it is important to acknowledge that our experiments were conducted in a natural stream system that inherently possesses uncharacterized heterogeneity, including variations in hydraulic conductivity, wetted perimeter, permeability of logjams, and other difficult-to-quantify characteristics that can influence solute transport processes. Although we attempted to isolate the effects of logjams and secondary channels, these inherent differences between reaches introduce additional variability and potentially confound the direct influence of logjam distribution or secondary channels on transient storage and hyporheic exchange. Furthermore, the hydrological connectivity and flow dynamics from Reach 1 influence the conditions and transport processes observed downstream in Reach 2, causing some degree of autocorrelation that may obscure the direct comparison between reaches with different logjam distributions; these ideas could be explored more fully in numerical models.

There are also experimental limitations to this work. It is also important to acknowledge our small sample size (i.e., two reaches). The two reaches compared in this study also had slightly different reach lengths and notably different transport distances to the upper transect from the injection point given thick vegetation that limited access to the stream in areas without other logjams. Ideally, the reach length would be similar when comparing breakthrough curve shape. We also did not have continuous data on the input concentrations—data were checked manually during injection with a handheld probe between each tracer-injection tank. Truncation, noise, and secondary peaks in instream EC and subsurface σ_{ba} BTCs introduce uncertainties in estimating behavior of solute transport from moment analysis. Duration and continuity of monitoring were partly constrained by the need to avoid summer convective storms and lightning, which were a near-daily occurrence at the field site. But these issues with the BTCs also lead to one conclusion of this paper, which perhaps should be obvious: simple statistics based on unimodal distributions may not perform well. Consequently, in many cases in this work, the estimated moments are not reasonable, leading to our reliance on more qualitative interpretation of the BTCs. Lastly, we did not have measurements everywhere we would have liked. Because we did not instrument the secondary channels with transducers, we regrettably did not completely capture the dynamics of the secondary channels in the field. Additionally, the cobble-laden substrate made the insertion of shallow piezometers impossible by hand, and we were working in a wilderness area where power equipment such as drills are not allowed.

Complex natural systems like those studied here are difficult to measure, and similarly difficult to model. The use of flume and numerical models to support field findings, where possible, is helpful in characterizing the heterogeneity of behaviors—in space and time—that cannot easily be captured in the field. But we note that systems with multiple channels (some of which are intermittent), multiple logjams, and backwater pools of evolving size require complex physical or numerical models to explore. This work opens a number of questions that could be studied with such models in terms of controls on surface and subsurface retention with discharge as well as how stream intermittency drives HEF; we explore these questions in detail numerically in Zhang et al. (n.d.), using HydroGeoSphere.

4. Conclusions

Our study provides insights into the complexity of transient storage in a natural stream system by comparing a reach characterized by two logjams and an intermittent secondary channel to a reach with a single logjam and a perennial secondary channel. Through three tracer tests conducted across varying discharges, we observed that stream intermittency and presence of logjams influence solute transport processes and the extent of transient storage. As discharge increases, the increased size of backwater pools and activation of a secondary channel in Reach 1 promotes surface transient storage, thereby increasing the potential for hyporheic exchange by increasing stream stage. At medium discharge, this newly flowing secondary channel and increased subsurface-flow path distribution, as observed through ER surveys, enhanced system heterogeneity. However, σ_{ba} BTCs and ER inversions demonstrate that while tracer movement into the subsurface increases with discharge and the hyporheic zone expands laterally and vertically with higher discharge, especially as the secondary channel starts to flow in Reach 1, subsurface flushing of solutes is highest at medium flow, resulting in low solute retention in contrast to the hypothesized response. As the flow in the secondary stream continues to increase at higher discharge, stagnant surface water is reduced.

This study represents one of the first attempts to investigate transient storage in a complex, natural stream system with multiple logjams and channels where stream intermittency adds a complicating factor. A conceptual model based on our findings highlights the control of intermittent secondary channels on both surface and subsurface transient storage. In short, logjams enhance stream corridor complexity and promote transient storage, but there are notable challenges, described above, in characterizing these processes in the field.

Overall, this research contributes to our understanding of transient storage in complex stream systems and highlights the significance of logjams for stream dynamics. The findings partially support our hypotheses: as expected, the reach with two logjams and an intermittent secondary channel exhibited greater variation in surface transient storage compared to the reach with a single logjam and a perennial side channel; however, differences in subsurface transient storage are less clear. While hyporheic exchange increases with discharge in both reaches, subsurface retention of solute was lowest for medium flow, contrary to expectations, due to a tradeoff between increasing extent and velocity of hyporheic flow as pressure gradients increased with surface discharge.

Further studies in natural channels with differing patterns of spatial heterogeneity may help to inform understanding of the relative importance of different types (e.g., bedforms vs. obstructions vs. channel bifurcations) and different magnitudes of heterogeneity (e.g., two subparallel channels vs. three, or five logjams per 100 m of channel vs. two). Our results support the idea that greater spatial heterogeneity generally equates to greater transient storage, although limits or thresholds may exist. Either way, river management and conservation efforts should prioritize the preservation and promotion of large wood and channel complexity in stream systems. By doing so, we can potentially enhance the overall health and functioning of these ecosystems, considering the positive influence of large wood on channel complexity and the associated enhancement of surface and subsurface transient-storage processes, however complex or nonlinear.

Conflict of Interest

The authors declare no conflicts of interest relevant to this study.

Data Availability Statement

All modified deconvolution codes are written in MATLAB and may be found, along with the data, on CUAHSI's HydroShare at http://www.hydroshare.org/resource/5535e4618ce545f5a66087ca784d7150. The deconvolution codes can also be found at https://zenodo.org/doi/10.5281/zenodo.10654912.

Acknowledgments
This material is based upon work supported by the National Science Foundation under Grants EAR-1819134 (KS), EAR-1819068 (EW), and EAR-2012730 (KS and ANS). We would like to thank Audrey Sawyer and Xiaolang Zhang for multiple useful conversations on the topic of retention, Jackie Randell and Stefan Klingler for support in the field, Garrett Wright for early efforts looking at the electrical resistivity data, and everyone who helped carry salt and equipment into the research site: Kaitlyn Berckman, Emily Iskin, Luke Jacobsen, Marissa Karpack, John Kemper, Zachary Kornse, Sarah Lowe, Chloe Roth, Julianne Scamardo, Isabella Schalko, Kenny Swift Bird, Danny White, and Karl Wilhelmsen. This manuscript benefited from comments by the associate editor and five reviewers, including Stanley Grant and John M. Buffington.

References

Ader, E., Wohl, E., McFadden, S., & Singha, K. (2021). Logjams as a driver of transient storage in a mountain stream. *Earth Surface Processes and Landforms*, *46*(3), 701–711. https://doi.org/10.1002/esp.5057

Beckman, N. D., & Wohl, E. (2014). Effects of forest stand age on the characteristics of logjams in mountainous forest streams. *Earth Surface Processes and Landforms*, *39*(11), 1421–1431. https://doi.org/10.1002/esp.3531

Bentley, L. R., & Gharibi, M. (2004). Two- and three-dimensional electrical resistivity imaging at a heterogeneous remediation site. *Geophysics*, *69*(3), 674–680. https://doi.org/10.1190/1.1759453

Bethune, J., Randell, J., Runkel, R. L., & Singha, K. (2015). Non-invasive flow path characterization in a mining-impacted wetland. *Journal of Contaminant Hydrology*, *183*, 29–39. https://doi.org/10.1016/j.jconhyd.2015.10.002

Binley, A., & Kemna, A. (2005). DC resistivity and induced polarization methods. In Y. Rubin & S. S. Hubbard (Eds.), *Hydrogeophysics* (Vol. 50, pp. 129–156). Springer. https://doi.org/10.1007/1-4020-3102-5_5

Blanchy, G., Saneiyan, S., Boyd, J., McLachlan, P., & Binley, A. (2020). ResIPy, an intuitive open source software for complex geoelectrical inversion/modeling. *Computers & Geosciences*, *137*, 104423. https://doi.org/10.1016/j.cageo.2020.104423

Buffington, J. M., & Tonina, D. (2009). Hyporheic exchange in mountain rivers II: Effects of channel morphology on mechanics, scales, and rates of exchange. *Geography Compass*, *3*(3), 1038–1062. https://doi.org/10.1111/j.1749-8198.2009.00225.x

Cirpka, O. A., Fienen, M. N., Hofer, M., Hoehn, E., Tessarini, A., Kipfer, R., & Kitanidis, P. K. (2007). Analyzing Bank filtration by deconvoluting time series of electric conductivity. *Groundwater*, *45*(3), 318–328. https://doi.org/10.1111/j.1745-6584.2006.00293.x

Day-Lewis, F. D., Singha, K., & Binley, A. M. (2005). Applying petrophysical models to radar travel time and electrical resistivity tomograms: Resolution-dependent limitations. *Journal of Geophysical Research*, *110*(B8). https://doi.org/10.1029/2004JB003569

Doughty, M., Sawyer, A. H., Wohl, E., & Singha, K. (2020). Mapping increases in Hyporheic exchange from channel-spanning logjams. *Journal of Hydrology*, *587*, 124931. https://doi.org/10.1016/j.jhydrol.2020.124931

Fischer, H., Kloep, F., Wilzcek, S., & Pusch, M. T. (2005). A river's liver—Microbial processes within the hyporheic zone of a large lowland river. *Biogeochemistry*, *76*(2), 349–371. https://doi.org/10.1007/s10533-005-6896-y

Geuzaine, C., & Remacle, J.-F. (2009). GMSH: A 3-D finite element mesh generator with built-in pre- and post-processing facilities. *International Journal for Numerical Methods in Engineering*, *79*(11), 1309–1331. https://doi.org/10.1002/nme.2579

Gippel, C. J. (1995). Environmental hydraulics of large woody debris in streams and rivers. *Journal of Environmental Engineering*, *121*(5), 388–395. https://doi.org/10.1061/(ASCE)0733-9372(1995)121:5(388)

González-Pinzón, R., Dorley, J., Singley, J., Singha, K., Gooseff, M., & Covino, T. (2022). TIPT: The Tracer Injection Planning Tool. *Environmental Modelling & Software*, *156*, 105504. https://doi.org/10.1016/j.envsoft.2022.105504

Gónzalez-Pinzón, R., Haggerty, R., & Dentz, M. (2013). Scaling and predicting solute transport processes in streams. *Water Resources Research*, *49*(7), 4071–4088. https://doi.org/10.1002/wrcr.20280

Gooseff, M. N., Benson, D. A., Briggs, M. A., Weaver, M., Wollheim, W., Peterson, B., & Hopkinson, C. S. (2011). Residence time distributions in surface transient storage zones in streams: Estimation via signal deconvolution. *Water Resources Research*, *47*(5), W05509. https://doi.org/10.1029/2010WR009959

Gooseff, M. N., Hall, R. O., Jr., & Tank, J. L. (2007). Relating transient storage to channel complexity in streams of varying land use in Jackson Hole, Wyoming. *Water Resources Research*, *43*(1). https://doi.org/10.1029/2005WR004626

Grant, S. B., Azizian, M., Cook, P., Boano, F., & Rippy, M. A. (2018). Factoring stream turbulence into global assessments of nitrogen pollution. *Science*, *359*(6381), 1266–1269. https://doi.org/10.1126/science.aap8074

Gupta, A., & Cvetkovic, V. (2000). Temporal moment analysis of tracer discharge in streams: Combined effect of physicochemical mass transfer and morphology. *Water Resources Research*, *36*(10), 2985–2997. https://doi.org/10.1029/2000wr900190

Harvey, C. F., & Gorelick, S. M. (1995). Temporal moment-generating equations: Modeling transport and mass transfer in heterogeneous aquifers. *Water Resources Research*, *31*(8), 1895–1911. https://doi.org/10.1029/95wr01231

Harvey, J. W., Wagner, B. J., & Bencala, K. E. (1996). Evaluating the reliability of the stream tracer approach to characterize stream-subsurface water exchange. *Water Resources Research*, *32*(8), 2441–2451. https://doi.org/10.1029/96wr01268

Hayley, K., Bentley, L. R., Gharibi, M., & Nightingale, M. (2007). Low temperature dependence of electrical resistivity: Implications for near surface geophysical monitoring. *Geophysical Research Letters*, *34*(18), L18402. https://doi.org/10.1029/2007GL031124

Hayley, K., Bentley, L. R., & Pidlisecky, A. (2010). Compensating for temperature variations in time-lapse electrical resistivity difference imaging. *Geophysics*, *75*(4), WA51–WA59. https://doi.org/10.1190/1.3478208

Hoagland, B., Navarre-Sitchler, A., Cowie, R., & Singha, K. (2020). Groundwater–stream connectivity mediates metal(loid) geochemistry in the hyporheic zone of streams impacted by historic mining and acid rock drainage. *Frontiers in Water*, *2*. https://doi.org/10.3389/frwa.2020.600409

Huang, S. H., & Yang, J. Q. (2023). Impacts of channel-spanning log jams on hyporheic flow. *Water Resources Research*, *59*(11), e2023WR035217. https://doi.org/10.1029/2023wr035217

Kaufman, M. H., Cardenas, M. B., Buttles, J., Kessler, A. J., & Cook, P. L. M. (2017). Hyporheic hot moments: Dissolved oxygen dynamics in the hyporheic zone in response to surface flow perturbations. *Water Resources Research*, *53*(8), 6642–6662. https://doi.org/10.1002/2016WR020296

Kaufmann, P. R., & Faustini, J. M. (2012). Simple measures of channel habitat complexity predict transient hydraulic storage in streams. *Hydrobiologia*, *685*(1), 69–95. https://doi.org/10.1007/s10750-011-0841-y

Keller, G. V., & Frischknecht, F. C. (1966). *Electrical methods in geophysical prospecting*. Elsevier Science & Technology.

Krause, S., Abbott, B. W., Baranov, V., Bernal, S., Blaen, P., Datry, T., et al. (2022). Organizational principles of hyporheic exchange flow and biogeochemical cycling in river networks across scales. *Water Resources Research*, *58*(3). https://doi.org/10.1029/2021WR029771

LaBrecque, D. J., & Yang, X. (2001). Difference inversion of ERT data: A fast inversion method for 3-D in situ monitoring. *Journal of Environmental & Engineering Geophysics*, *6*(2), 83–89. https://doi.org/10.4133/JEEG6.2.83

Livers, B., & Wohl, E. (2016). Sources and interpretation of channel complexity in forested subalpine streams of the Southern Rocky Mountains: Channel complexity in forested streams. *Water Resources Research*, *52*(5), 3910–3929. https://doi.org/10.1002/2015WR018306

Magliozzi, C., Grabowski, R. C., Packman, A. I., & Krause, S. (2018). Toward a conceptual framework of hyporheic exchange across spatial scales. *Hydrology and Earth System Sciences*, *22*(12), 6163–6185. https://doi.org/10.5194/hess-22-6163-2018

Mao, L., Andreoli, A., Comiti, F., & Lenzi, M. A. (2008). Geomorphic effects of large wood jams on a sub-Antarctic mountain stream. *River Research and Applications*, *24*(3), 249–266. https://doi.org/10.1002/rra.1062

Marshall, A., Zhang, X., Sawyer, A. H., Wohl, E., & Singha, K. (2023). Logjam characteristics as drivers of transient storage in headwater streams. *Water Resources Research*, *59*(3), e2022WR033139. https://doi.org/10.1029/2022WR033139

Marzadri, A., Tonina, D., Bellin, A., & Valli, A. (2016). Mixing interfaces, fluxes, residence times and redox conditions of the Hyporheic zones induced by dune-like Bedforms and ambient groundwater flow. *Advances in Water Resources*, *88*, 139–151. https://doi.org/10.1016/j.advwatres.2015.12.014

Marzadri, A., Tonina, D., McKean, J. A., Tiedemann, M. G., & Benjankar, R. M. (2014). Multi-scale streambed topographic and discharge effects on hyporheic exchange at the stream network scale in confined streams. *Journal of Hydrology*, *519*, 1997–2011. https://doi.org/10.1016/j.jhydrol.2014.09.076

Mason, S. J. K., McGlynn, B. L., & Poole, G. C. (2012). Hydrologic response to channel reconfiguration on silver bow creek, Montana. *Journal of Hydrology*, *438*(439), 125–136. https://doi.org/10.1016/j.jhydrol.2012.03.010

Nimmer, R. E., Osiensky, J. L., Binley, A. M., & Williams, B. C. (2008). Three-dimensional effects causing Artifacts in two-dimensional, cross-borehole, electrical imaging. *Journal of Hydrology*, *359*(1–2), 59–70. https://doi.org/10.1016/j.jhydrol.2008.06.022

Oldenburg, D. W., & Li, Y. (1999). Estimating depth of investigation in dc resistivity and IP surveys. *Geophysics*, *64*(2), 403–416. https://doi.org/10.1190/1.1444545

Payn, R. A., Gooseff, M. N., Benson, D. A., Cirpka, O. A., Zarnetske, J. P., Bowden, W. B., et al. (2008). Comparison of instantaneous and constant-rate stream tracer experiments through non-parametric analysis of residence time distributions. *Water Resources Research*, *44*(6), W06404. https://doi.org/10.1029/2007WR006274

Runkel, R. L. (2002). A new metric for determining the importance of transient storage. *Journal of the North American Benthological Society*, *21*(4), 529–543. https://doi.org/10.2307/1468428

Salehin, M., Packman, A. I., & Paradis, M. (2004). Hyporheic exchange with heterogeneous streambeds: Laboratory experiments and modeling. *Water Resources Research*, *40*(11). https://doi.org/10.1029/2003WR002567

Sawyer, A. H., Bayani Cardenas, M., & Buttles, J. (2011). Hyporheic exchange due to channel-spanning logs. *Water Resources Research*, *47*(8), 1–12. https://doi.org/10.1029/2011WR010484

Sawyer, A. H., & Cardenas, M. B. (2012). Effect of experimental wood addition on hyporheic exchange and thermal dynamics in a losing meadow stream. *Water Resources Research*, *48*(September), 1–11. https://doi.org/10.1029/2011WR011776

Schalko, I., Ponce, M., Lassar, S., Schwindt, S., Haun, S., & Nepf, H. (2024). Flow and turbulence due to wood contribute to declogging of gravel bed. *Geophysical Research Letters*, *51*(2), e2023GL107507. https://doi.org/10.1029/2023GL107507

Singha, K., & Gorelick, S. M. (2006). Effects of spatially variable resolution on field-scale estimates of tracer concentration from electrical inversions using Archie's law. *Geophysics*, *71*(3), G83–G91. https://doi.org/10.1190/1.2194900

Singley, J. G., Singha, K., Gooseff, M. N., González-Pinzón, R., Covino, T. P., Ward, A. S., et al. (2022). Identification of hyporheic extent and functional zonation during seasonal streamflow recession by unsupervised clustering of time-lapse electrical resistivity models. *Hydrological Processes*, *36*(10). https://doi.org/10.1002/hyp.14713

Tonina, D., & Buffington, J. M. (2009). Hyporheic exchange in mountain rivers I: Mechanics and environmental effects: Mechanics of hyporheic exchange. *Geography Compass*, *3*(3), 1063–1086. https://doi.org/10.1111/j.1749-8198.2009.00226.x

Tonina, D., & Buffington, J. M. (2011). Effects of stream discharge, alluvial depth and bar amplitude on hyporheic flow in pool-riffle channels: Hyporheic flow in pool-riffle channels. *Water Resources Research*, *47*(8). https://doi.org/10.1029/2010WR009140

Vanderborght, J., Kemna, A., Hardelauf, H., & Vereecken, H. (2005). Potential of electrical resistivity tomography to infer aquifer transport characteristics from tracer studies: A synthetic case study: Monitoring of a tracer test using ert. *Water Resources Research*, *41*(6). https://doi.org/10.1029/2004WR003774

Ward, A. S., Gooseff, M. N., & Singha, K. (2010a). Characterizing hyporheic transport processes—Interpretation of electrical geophysical data in coupled stream-hyporheic zone systems during solute tracer studies. *Advances in Water Resources*, *33*(11), 1320–1330. https://doi.org/10.1016/j.advwatres.2010.05.008

Ward, A. S., Gooseff, M. N., & Singha, K. (2010b). Imaging Hyporheic zone solute transport using electrical resistivity. *Hydrological Processes*, *24*(7), 948–953. https://doi.org/10.1002/hyp.7672

Ward, A. S., Payn, R. A., Gooseff, M. N., McGlynn, B. L., Bencala, K. E., Kelleher, C. A., et al. (2013). Variations in surface water-ground water interactions along a headwater mountain stream: Comparisons between transient storage and water balance analyses. *Water Resources Research*, *49*(6), 3359–3374. https://doi.org/10.1002/wrcr.20148

Wilhelmsen, K., Sawyer, A., Marshall, A., McFadden, S., Singha, K., & Wohl, E. (2021). Laboratory flume and numerical modeling experiments show log jams and branching channels increase hyporheic exchange. *Water Resources Research*, *57*(9). https://doi.org/10.1029/2021WR030299

Wlostowski, A. N., Gooseff, M. N., Bowden, W. B., & Wollheim, W. M. (2017). Stream tracer breakthrough curve decomposition into mass fractions: A simple framework to analyze and compare conservative solute transport processes. *Limnology and Oceanography: Methods*, *15*(2), 140–153. https://doi.org/10.1002/lom3.10148

Wohl, E. (2005). Compromised rivers: Understanding historical human impacts on rivers in the context of restoration. *Ecology and Society*, *10*(2), art2. https://doi.org/10.5751/ES-01339-100202

Wohl, E. (2006). Human impacts to mountain streams. *Geomorphology*, *79*(3–4), 217–248. https://doi.org/10.1016/j.geomorph.2006.06.020

Wohl, E. (2014). A legacy of absence: Wood removal in US rivers. *Progress in Physical Geography: Earth and Environment*, *38*(5), 637–663. https://doi.org/10.1177/0309133314548091

Wohl, E. (2017). Geomorphology Bridging the gaps: An overview of wood across time and space in diverse rivers. *Geomorphology*, *279*, 3–26. https://doi.org/10.1016/j.geomorph.2016.04.014

Wohl, E., Marshall, A. E., Scamardo, J., White, D., & Morrison, R. R. (2022). Biogeomorphic influences on river corridor resilience to wildfire disturbances in a mountain stream of the Southern Rockies, USA. *The Science of the Total Environment*, *820*, 153321. https://doi.org/10.1016/j.scitotenv.2022.153321

Wohl, E., & Scamardo, J. E. (2021). The resilience of logjams to floods. *Hydrological Processes*, *35*(1). https://doi.org/10.1002/hyp.13970

Wroblicky, G. J., Campana, M. E., Valett, H. M., & Dahm, C. N. (1998). Seasonal variation in surface- subsurface water exchange and lateral hyporheic area of two stream-aquifer systems. *Water Resources Research*, *34*(3), 317–328. https://doi.org/10.1029/97wr03285

Young, D. F., & Ball, W. P. (2000). Column experimental design requirements for estimating model parameters from temporal moments under nonequilibrium conditions. *Advances in Water Resources*, *23*(5), 449–460. https://doi.org/10.1016/s0309-1708(99)00047-0

Zhang, N., Rutherfurd, I. D., & Ghisalberti, M. (2020). The effect of instream logs on bank erosion potential: A flume study with multiple logs. *Journal of Ecohydraulics*, *5*(1), 57–70. https://doi.org/10.1080/24705357.2019.1669495

Zhang, X., Sawyer, A. H., Singha, K., & Wohl, E. (n.d.). *Exploring the influence of morphologic heterogeneity and discharge on transient storage in stream systems: 2. Insights from numerical models*. Submitted to Water Resources Research.

References From the Supporting Information

Kitanidis, P. K. (1999). Generalized covariance functions associated with the Laplace equation and their use in interpolation and inverse problems. *Water Resources Research*, *35*(5), 1361–1368. https://doi.org/10.1029/1999wr900026